Phase separation in nanomaterials : development of models and simulation techniques

Bence Daniel Gajdics

Phase separation in nanomaterials - development of models and simulation techniques

Doctoral (PhD) dissertation

Bence Dániel B. Gajdics

Supervisors:
Prof. Zoltán Erdélyi and Prof. Helena Zapolsky

University of Debrecen
Doctoral Council of Natural Sciences and Information Technology
Doctoral School of Physics
Debrecen, 2020

Ezen értekezést a Debreceni Egyetem TTK *fizika tudományok* doktori iskola *szilárdtestfizika és anyagtudomány* programja keretében készítettem a Debreceni Egyetem TTK doktori (PhD) fokozatának elnyerése céljából.

Debrecen, 2020. . . . . .

B. Gajdics Bence Dániel

Tanúsítom, hogy *B. Gajdics Bence Dániel* doktorjelölt 2016 - 2020 között a fent megnevezett doktori iskola szilárdtestfizika és anyagtudomány programjának keretében irányításommal végezte munkáját. Az értekezésben foglalt eredményekhez a jelölt önálló alkotó tevékenységével meghatározóan hozzájárult. Az értekezés elfogadását javasolom.

Debrecen, 2020. . . . . .

Dr. Erdélyi Zoltán
témavezető

To my parents

How do you expect to communicate with the ocean,
when you can't even understand one another?
- Stanisław Lem, Solaris

Acknowledgements

First of all, I would like to express my gratitude and appreciation to my two supervisors, Prof. Zoltán Erdélyi and Prof. Helena Zapolsky. I am grateful for their outstanding professional mentorship and for their continuous support of my research with their expertise and personal experience.

I would also like to thank my two tutors, János Tomán and Gilles Demange, who guided me with their advices during our work together. I am also thankful to Prof. Andriy Gusak and his research group from the University of Cherkasy.

This thesis could have never been written without the support from Campus France, whose scholarship enabled me to pursue my joint doctoral studies at the University of Debrecen and at the University of Rouen. Thanks to Mr. Bob Kaba Loemba for his assistance. I would also like to thank Renaud Patte for his professional support and for his generous help with the administrative tasks.

I am grateful for the fincancial support of the French-Hungarian TéT_16_FR/Balaton project, the GINOP-2.3.2-15-2016-00041 project and the European Union and the European Regional Development Fund.

I am thankful to all the staff of the Department of Solid State Physics in Debrecen and the GPM group in Rouen for the opportunity to work in such great communities.

Finally, I would like to thank my family and friends and especially my parents for being there for me throughout this journey.

Contents

Introduction

In the recent decades, nanomaterials are in the forefront of ivestigations in the field materials science, due to their benefitial size-dependent properties in many instances. Phase separation on nanoscale, bimetallic nanoparticles consisting of one- or two-phases can be utilized in a wide range of fields from optical, chemical, catalytic, plasmonic to even biological applications, as a result of their good properties.

The formation of various metastable/unstable structures can be observed in systems alike and as a result of heat treatment, during or after the growth, these can go through spontaneous phase transformation or separation. By the proper description of such processes, one can face a plethora of possibilities for designing and regulating the atomistic structure of such materials and as a consequence, the properties of these nanoformations.

There is a huge interest in the field of materials science of modelling and computer simulation methods that can tackle the problems of dealing with the various processes of the nanoscale. These are either atomistic or continuum approaches and they are often combined, forming a multiscale procedure, in order to address the numerous dynamical processes lying behind the formation of complex microstructures.

The goal of my thesis is to present my contributions in the field of phase separation on the nanoscale by the development of atomistic models and new computer simulation techniques.

Chapter 1

Theoretical aspects

1.1 Phase separation in alloys

In 1958, Cahn and Hilliard described the free energy function for a cubic crystal or an isotropic, non-homogeneous binary medium in the following form [1]:

$$F = \rho \int_{\Omega} \left[f_0 + \kappa_1 \nabla^2 c + \kappa_2 (\nabla c)^2 + \cdots \right] \mathrm{d}\Omega, \tag{1.1}$$

where ρ is the total volume density (the number of molecules per unit volume), Ω is the volume, f_0 is the free energy per molecule of a solution of uniform composition c, κ_is are coefficients. It has been shown that by applying the divergence theorem, the number of coefficients κ can be reduced:

$$\int_{\Omega} \nabla(\kappa_1 \nabla c)\ \mathrm{d}\Omega = \oint_{S} \kappa_1 \nabla c\ \vec{n} \mathrm{d}S, \tag{1.2}$$

where $\vec{n}$ is the normal vector of the surface S. Since we are not concerned with the effects on the external surface, we can choose an integration limit on the right-hand side such that $\nabla c\, \vec{n}$ is zero at the boundary (∇c is perpendicular to the surface normal). The surface integral thus vanishes. Furthermore, by applying the left-hand side derivation rules (multiplication and

chain) we obtain:

$$\int_\Omega \kappa_1 \nabla^2 c \, \mathrm{d}\Omega + \int_\Omega \frac{d\kappa_1}{dc} (\nabla c)^2 \mathrm{d}\Omega = 0. \tag{1.3}$$

We can employ Eq. (1.3) to eliminate the term containing $\nabla^2 c$ from Eq. (1.1), which results in:

$$F = \rho \int_\Omega \left[f_0 + \kappa (\nabla c)^2 + \cdots \right] \mathrm{d}\Omega, \tag{1.4}$$

where:

$$\kappa = -\frac{d\kappa_1}{dc} + \kappa_2, \tag{1.5}$$

called gradient energy coefficient. Note that usually the higher order terms are neglected in Eq. (1.4).

In the simplest case a regular solid solution is considered:

$$\begin{aligned} f_0 = {} & f_A c + f_B (1-c) + c(1-c) V_0 \\ & + kT[c \ln(c) + (1-c) \ln(1-c)], \end{aligned} \tag{1.6}$$

where V_0 is the regular solid solution parameter and for this case Cahn and Hilliard determined the values of κ_1 and κ_2 [1]:

$$\kappa_{1R} = -c \frac{\xi^2 V_0}{2} \quad \text{and} \quad \kappa_{2R} = 0, \tag{1.7}$$

where the subscript R denotes the value of the parameter for the regular solid solution, ξ is the effective interaction distance, and if interactions other than nearest-neighbour interactions are neglected, $\xi = r_0/\sqrt{3}$, where r_0 is the distance between atoms.

Hence, even in the simplest case – regular solid solution – κ_1 is composition dependent (linearly), and accordingly the gradient energy coefficient defined in equation Eq. (1.5) is:

$$\kappa_R = \frac{\xi^2 V_0}{2}. \tag{1.8}$$

Note that if κ_1 was not composition dependent we could not eliminate the term in $\nabla^2 c$ from Eq. (1.1), as a consequence to introduce the gradient energy coefficient κ.

As can be seen, the energy coefficient of the gradient is composition independent. It should be emphasized, however, that this result is valid only for a regular solid solution. In this work, the gradient energy coefficient will be determined for nonregular solid solutions. It is expected that for non-regular solid solutions, κ_1 is not only linearly dependent on the composition, so that κ will also be composition dependent. We will show that κ as a function of composition can be calculated from the interaction energy $V(c)$ of the solution – given by, e.g., the Redlich and Kister polynomial [2]. Note that there have been few attempts in the literature to account for the composition dependent κ due to its complexity (e.g. [3–5]), although the implications of this may not be negligible. It has been shown, for example, that the morphological evolution pathways and spinodal microstructure of polymer systems with highly asymmetric phase diagrams can be very different from those with symmetric phase diagrams [6]. The segregation energy is also expected to change, which plays an important role in solute segregation and segregation transition in extensive defects such as grain boundaries [7]. In this work, we also present some consequences of composition-dependent gradient energy coefficients.

Interdiffusion in the presence of a steep concentration gradient can be described by the Cahn-Hilliard theory. The atomic flux for a two component system in one dimension can be calculated:

$$j_A = -\tilde{D}\frac{\partial \rho_A}{\partial x} + \frac{2\tilde{D}\rho^2}{f_0''}\kappa\frac{\partial^3 \rho_A}{\partial x^3}, \tag{1.9}$$

where $\tilde{D}$ is the interdiffusion coefficient. and

$$f_0'' = \frac{\partial^2 f_0}{\partial c_A^2}. \tag{1.10}$$

In this case, the atomic flux does depend on the concentration gradient and on the third gradient term. The free energy, for a homogeneous binary alloy in mean-field approximation, depends only on the concentration of one component ($F = F(c)$). In order to being able to describe non-homogeneous solid solutions, the free energy has to depend on the inhomogenities also, that is on the gradient of the composition. Cahn and Hilliard did not go further than the second order terms. If we substitute Eq. (1.9) into the equation of conservation of matter, then:

$$\frac{\partial \rho_A}{\partial t} = \tilde{D}\frac{\partial^2 \rho_A}{\partial x^2} - \frac{2\tilde{D}\rho^2}{f_o''}\kappa\frac{\partial^4 \rho_A}{\partial x^4}. \tag{1.11}$$

When κ equals zero, the system can be treated as an ideal solid solution. In the $\kappa > 0$ case, phase separation can be observed, while $\kappa < 0$ results in ordering. Note that, the interdiffusion coefficient can be expressed using f_0'' and the mobility $\mathcal{M}$, can only be positive or zero value:

$$\tilde{D} = \frac{1}{\rho}\mathcal{M}f_0''. \tag{1.12}$$

A particular solution of Eq. (1.11) is assumed to have the form of

$$\rho_A(t) - \rho_A^0 = A(t)\sin(hx) \tag{1.13}$$

and $h = 2\pi/\lambda$, where λ is the modulation length and this gives:

$$R = \frac{d\ln A}{dt} = -\tilde{D}\left[1 + \frac{2\kappa h^2}{f_0''}\rho^2\right]h^2. \tag{1.14}$$

This shows that for a given values of κ and f_0'', the A amplitude of a λ

wavelength fluctuation increases or decreases with time, i.e. the solution is in the direction of decomposition/separation or not. In the ideal case, $\kappa = 0$, $f_0'' > 0$ and A decreases. In phase separating systems, κ is always positive, but f_0'' changes sign as a function of temperature and composition.

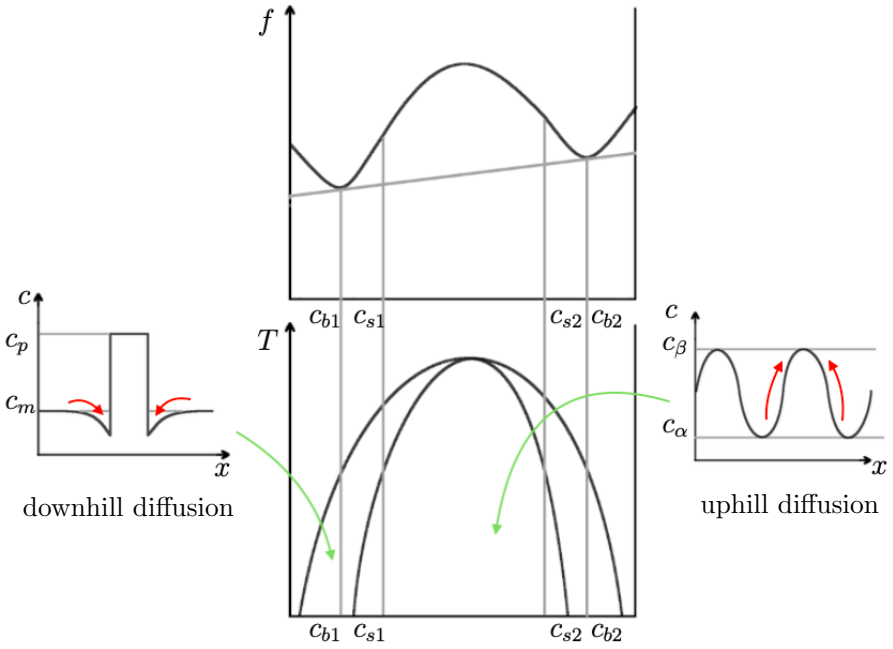

Figure 1.1: Schematic representation of the free energy curve on a given temperature and the miscibility gap with the spinodal curve inside, which separates the metastable ($f_0'' > 0$) and unstable ($f_0'' < 0$) region. The figure on the left shows the mechanism of the nucleation and growth process (c_p: composition of precipitate, c_m: composition of matrix). On the right, one can see the schematic view of the spinodal decomposition, where $(c_\alpha - c_\beta) = 2A < (c_{s2} - c_{s1})$.

The free energy curve defines that on a specific temperature which compositions are the solubility limits. As Fig.1.1 shows c_{b1} and c_{b2} are the corresponding compositions, where a common tagent connects the two-minima

free energy function. The inflection points, where f_0'' changes signs, are c_{s1} and c_{s2}. By tracking these parameters, while changing the temperature, a map can be created, forming the binodal and spinodal curves.

Inside the spinodal curve $f_0'' < 0$ and $j = -\tilde{D}\frac{\partial \rho}{\partial x}$ the atomic flux goes to the the direction of the concentration gradient. This phenomenon is called spinodal decomposition. The random fluctuations above λ_c critical wavelength start to grow. When the material is cooled down to this region, it is in an unstable state. Fluctuations appear and it decomposes into A and B rich regions. The fluctuations grow until they reach the concentrations corresponding to the miscibility gap (c_{b1} and c_{b2}) by the so called *uphill diffusion*. After that, coarsening process takes place, beacuse the large number of interfaces between the phases are energetically unfavourable. Note that $\lambda_m = \sqrt{2}\lambda_c$ is the fastest growing wavelength.

Outside of the spinodal curve ($f_0'' > 0$) is a metastable region, where the nucleation-growth-coarsening process can take place. In that case, contrary to the spinodal decomposition, *downhill diffusion* can be observed.

1.2 Methods

1.2.1 Phase field model

In the phase-field model, the microstructure of the decomposing binary A-B system is described by the coarse grained concentration $c(\boldsymbol{r}, t)$ of component A. The temporal evolution of this concentration field is then given by the phase field equation, also called Cahn-Hilliard equation [8]:

$$\frac{\partial c}{\partial t} = \nabla \left(\mathcal{M} \nabla \left[\frac{\delta F(c)}{\delta c} \right] \right). \tag{1.15}$$

Here, $\mathcal{M}$ is the atomic mobility, and $F(c)$ is the total non-equilibrium free energy on the volume Ω, which embodies the bulk free energy and the interfacial energy [9]:

$$F = \rho \int_{\Omega} \left[f_0(c) + \kappa |\nabla c|^2 \right] \mathrm{d}\Omega. \tag{1.16}$$

To model the kinetics of spinodal decomposition in the PFM, the phase-field equation 1.15 is numerically solved in its reduced form. For that purpose, the reduced free energy potential f_0^* is expressed in units of $k_B T$:

$$\begin{aligned} f_0^*(c) = c(1-c) \left[\frac{V_0}{k_B T} + \frac{V_1}{k_B T}(2c-1) \right] \\ + \left[c \ln c + (1-c) \ln(1-c) \right]. \end{aligned} \tag{1.17}$$

Besides, on introducing the characteristic time and length scales t_0 and l_0, the PFM reduced time is $t^*_{\mathrm{PFM}} = t/t_0$, and the reduced gradient operator is $\nabla^* = l_0 \nabla$. Setting $t_0 = 2\kappa/(\kappa^* \mathcal{M}(k_B T)^2)$, and $l_0 = \sqrt{2\kappa/(\kappa^* k_B T)}$, where κ^* sets the reduced width of diffuse interfaces between phases, the reduced phase-field equation is:

$$\frac{\partial c}{\partial t^*} = (\nabla^*)^2 \left[\ln\left(\frac{c}{1-c} \right) + a_1 c^2 + a_2 c - \kappa^* (\nabla^*)^2 c \right], \tag{1.18}$$

where $a_1 = -6V_1/(k_B T)$, $a_2 = (6V_1 - 2V_0)/(k_B T)$ from the first derivative of $f_0^*(c)$ in equation 1.17. Here, the mobility is assumed constant, as it was justified for the Ag-Cu system in [10].

1.2.2 (Stochastic) kinetic mean-field model

In order to help the reader better understand the idea behind the three-dimensional stochastic kinetic mean field model, first of all George Martin's one-dimesnional kimetic mean-field model is going to be presented in the following section. Thus, these results are not outcomes of this dissertation, rather than a summary and overview of previous works.

1D Kinetic mean-field

George Martin proposed a one-dimensional Kinetic Mean-Field model. In this method, a given sample is being treated as planes of a three-dimensional sample. Atomic movements are only permitted between the planes, but intraplanar diffusion does not change the microstate. In the case of a two-component system (where A and B atoms are present) only the exchange of the two sorts between two neighbouring planes are changing the atomic configuration. Otherwise the system remains untouched.

Let us take a one-dimensional set of planes with the corresponding concentrations. The c_i concentration is the atomic fraction of a given sort on the plane i. The neighbouring planes can be described as c_{i-1} and c_{i+1}. To describe the rate of change of the concentration between the planes, Martin calculates the atomic flux or net flux [11] between the neighbouring planes. $J_{i-1,i}$ is the incoming whereas $J_{i,i+1}$ is the outgoing flux compared to the reference plane i. Thus, in the case of positive values of atomic fluxes, $J_{i-1,i}$ increases, $J_{i,i+1}$ decreases the atomic fraction of A on plane i. Based on this, one can get to the following equation:

$$\frac{dc_i}{dt} = J_{i-1,i} - J_{i,i+1}. \tag{1.19}$$

The number of jumps per unit time must be known to calculate the atomic fluxes, or in other words the number of exchanges per unit time. This value is noted as Γ. In 1990 George Martin [11] found a criterion for the selection of Γ, which brings the system in a thermodynamic equillibrium. This indicates that the model is deterministic, because the system will always lead to a thermodynamic equilibrium.

Hence, the goal is to find the concentration profile which corresponds to the thermodynamic equilibrium. But there are two ways to find it: a thermodynamic and a kinetic way. The thermodynamic consideration gives us the final configuration, on the other hand, the kinetic considerations

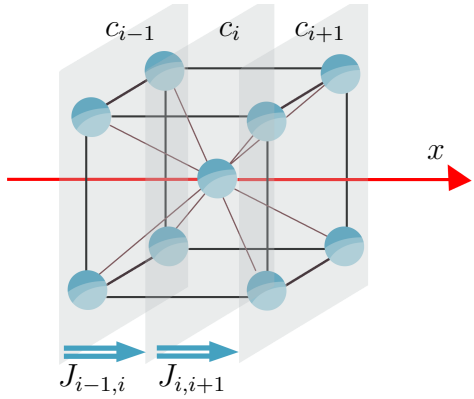

Figure 1.2: Atomic planes along the direction of the x axis, the corresponding c_{i-1}, c_i, c_{i+1} atomic fractions are indicated and the $J_{i-1,i}$, $J_{i,i+1}$ atomic fluxes.

are showing the intermediate states which the system goes through while getting to the equilibrium state. One can say that the system is in an equilibrium state, when the free energy function has a minimum, thus the thermodynamic method minimizes the free energy and the other method solves the kinetic equations.

If the Γ jump frequency is known, the $J_{i,i+1}$ atomic fluxes can be determined as well. To change the atomic configuration an A and a B atom have to change places between plane i and $i+1$: site i has to contain an A and site $i+1$ a B atom, or the other way around. The probability that a randomly chosen atom from plane i is A, is exactly c_i, which comes from the definition of the atomic fraction $c_i = N_i^A/N$. It shows what is the proportion of A atoms on a plane containing N atoms. The probability of finding a B atom on a neighbouring $i+1$ plane is $(1-c_{i+1})$ and these probabilities are independent. We need to know the $\Gamma_{i,i+1}$ frequency. These are the jumps pushing the A atoms into the x direction. In the opposite direction, an A atom from the plane $i+1$ and B atom from plane i switches places. The corresponding jump frequency is $\Gamma_{i+1,i}$. We need to take into

account, that a chosen atom from a plane can change places with more than one atom from the neighboring planes. This is noted with Z_v, e.g. vertical coordination number and it gives the number of nearest neighboring sites. The value of Z_v depends on the crystallography and the orientation of our sample alloy. By using the previous scheme:

$$J_{i,i+1} = Z_v \left[c_i(1-c_i)\Gamma_{i,i+1} - c_{i+1}(1-c_i)\Gamma_{i+1,i} \right]. \tag{1.20}$$

Using Eq.(1.20), the change of rate of the concentration Eq.(1.19)can be evaluated. According to Martin, the Γ must be chosen in a way, that in the state corresponding to the thermodynamic equilibrium, all of the atomic fluxes have to be zero:

$$J_{i,i+1} = 0 \qquad \forall \quad i. \tag{1.21}$$

In a thermodynamic equilibrium there are no atomic fluxes. Hence, based on Eq.(1.19) and Eq.(1.21) this gives us:

$$c_i(1-c_{i+1})\Gamma_{i,i+1} = c_{i+1}(1-c_i)\Gamma_{i+1,i}, \tag{1.22}$$

which can be reformulated as:

$$\frac{c_i(1-c_{i+1})}{c_{i+1}(1-c_i)} = \frac{\Gamma_{i,i+1}}{\Gamma_{i+1,i}}, \tag{1.23}$$

and it is called the *detailed balance condition*. We can get until this point by using kinteic equations.

The system has to get into a thermodynamic equilibrium when the free energy has a minimum and this is a sufficient condition:

$$F = U - TS, \tag{1.24}$$

where F is the free energy, U is the internal energy, T is the absolute temperature and S is the configurational enthropy. By dividing F with the

number of atoms in the system, we obtain the free energy per atom:

$$f = u - Ts. \tag{1.25}$$

In mean-field approximation, we can count the total free energy summarized for all planes in the system. The probability of finding an A atom on plane i is c_i, finding a B atom is $1 - c_i$ and the corresponding bond energies are E_i^A and E_i^B. This has to be devided by 1/2 to not count every pair twice, resulting in the internal energy per atom:

$$u = \frac{1}{2\mathcal{N}} \sum_{i=1}^{\mathcal{N}} \left[c_i E_i^A + (1 - c_i) E_i^B \right], \tag{1.26}$$

where $\mathcal{N}$ is the total number of planes in the system. The enthropy term in mean-field approximation and assuming a two component system:

$$s = -k_B \frac{1}{2\mathcal{N}} \left[c_i \ln c_i + (1 - c_i) \ln(1 - c_i) \right], \tag{1.27}$$

where k_B is the Boltzman constant. But the bond energy is still unknown. The bond energy of an A atom on plane i can be calculated the following way: the chosen atom has Z_v neighbors on plane $i - 1$. If they are A atoms, then the pair interaction energy is V_{AA}. The probability, that these neighbors are B atoms is $1 - c_{i-1}$ and the pair interaction energy is V_{AB}. Inside the given i plane, it has Z_l lateral neighbors, which is the lateral coordination number. We should take into consideration that wheather they are A or B atoms and multiply with the correct interaction energies the following terms. By continuing this idea to plane $i + 1$, the following

equation can be obtained:

$$\begin{aligned} E_i^A = & Z_v c_{i-1} V_{AA} + Z_v (1 - c_{i-1}) V_{AB} + \\ & + Z_l c_i V_{AA} + Z_l (1 - c_i) V_{AB} + \\ & + Z_v c_i V_{AA} + Z_l (1 - c_{i+1}) V_{AB} \end{aligned} \tag{1.28}$$

By reorganizing the equation we can get the A bond energy:

$$\begin{aligned} E_i^A = & Z_v \left[(c_{i-1} + c_{i+1}) V_{AA} + (2 - c_{i-1} - c_{i+1}) V_{AB} \right] + \\ & Z_l \left[c_i V_A A + (1 - c_i) V_{AB} \right]. \end{aligned} \tag{1.29}$$

Following the logic, the bond energy of B atoms can be calculated as:

$$\begin{aligned} E_i^B = & Z_v \left[(c_{i-1} + c_{i+1}) V_{AB} + (2 - c_{i-1} - c_{i+1}) V_{BB} \right] + \\ & Z_l \left[c_i V_A B + (1 - c_i) V_{BB} \right], \end{aligned} \tag{1.30}$$

where V_{BB} is the strength of a bond between two B atoms. Thus, we can say that by knowing E_i^A and E_i^B, g is a function which depends on every concentration from $c_1, \ldots, c_{\mathcal{N}}$:

$$f = f(c_1, \ldots, c_{\mathcal{N}}). \tag{1.31}$$

We have to minimize this function, by keeping the sum of c_i constant in the system:

$$\sum_{i=1}^{\mathcal{N}} c_i = \text{const.} \tag{1.32}$$

This is a conditional limit calculation. In the case of functions of several variables, there exist an extremum (maximum or minimum) only, if all the partial derivatives are zeros.

$$\frac{\partial f}{\partial c_1} = 0, \frac{\partial f}{\partial c_2} = 0, \ldots, \frac{\partial f}{\partial \mathcal{N}} = 0. \tag{1.33}$$

To find out whether it is a minimum or a maximum, we need to calculate the second derivative as well. The result is a system of equations consisting $\mathcal{N}$ equations which must be solved with the condition Eq.(1.32).

$$\frac{\partial f}{\partial c_i} = -2V\left[Zc_i + Z_v(c_{i+1} + c_{i-1} + 2c_i)\right] + kT\ln\frac{c_i}{1-c_i} \equiv \tilde{\mu}_i, \qquad (i = 2, \ldots, \mathcal{N}-1) \tag{1.34}$$

where Z is the total coordination number: $Z = 2Z_v + Z_l$ and $\tilde{\mu}_i$ is the exchange chemical potential. Surface effects are not taken into account in this case. V is the regular solid solution parameter:

$$V = V_{AB} - \frac{V_{AA} + V_{BB}}{2}. \tag{1.35}$$

Free energy has a minimum, when all the $\tilde{\mu}_i$ chemical potentials are equal with each other ($\tilde{\mu} = \tilde{\mu}_i \ \forall \ i.$) If this condition is true for all $\tilde{\mu}_i$, then $\tilde{\mu}_i = \tilde{\mu}_{i+1}$:

$$\begin{aligned} -2V\left[Zc_i + Z_v(c_{i+1} + c_{i-1} + 2c_i)\right] + kT\ln\frac{c_i}{1-c_i} = \\ -2V\left[Zc_{i+1} + Z_v(c_{i+2} + c_i + 2c_{i+1})\right] + kT\ln\frac{c_{i+1}}{1-c_{i+1}}. \end{aligned} \tag{1.36}$$

If Eq.(1.23) and Eq.(1.36) coincide, then the kinetic equations are leading to a thermodynamic balance, thus Γ has to be correctly selected. According to Martin [11], $\Gamma_{i,i+1}$ has an Arrhenius-type dependency on the temperature, because it is a thermally activated process:

$$\Gamma_{i,i+1} = \nu\exp\left(-\frac{E_{i,i+1}}{k_B T}\right), \tag{1.37}$$

where ν is the attempt frequency (proportional to the Debye frequency) and $E_{i,i+1}$ is the activation energy. We assume the atoms being trapped in a potential well, and the depth of the well is proportional how bounded an atom is in a given position energetically. It is important, that the A and

B atoms both must reach the E_0 saddlepoint energy to achive a successful exchange.

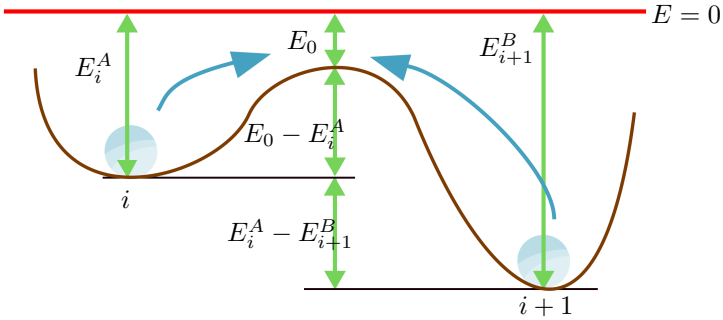

Figure 1.3: Schematic representation of the saddlepoint and bond energies.

The activation energy thus:

$$E_{i,i+1} = 2E^0 - E_i^A - E_{i+1}^B = 2E^0 - [Z_v(c_i + c_{i+2}) + Z_l c_{i+1}](V_{AB} - V_{BB}) + \\ + [Z_v(c_{i-1} + c_{i+1}) + Z_l c_i](V_{AB} - V_{AA}) - Z(V_{AB} + V_{BB}). \tag{1.38}$$

Martin had stopped somewhere here. He used such pair interaction energies. At the University of Debrecen Department of Solid State Physics, a model was created based on these result, which was mentioned as MEB (Martin - Erdélyi - Beke) model [12] in the scientific community. This model wanted to transform the pair interaction energies into an experimentally easily quantifiable result. By reformalising V, we can get the value of $V_{AB} - V_{AA}$:

$$V = V_{AB} - \frac{V_{AA} + V_{BB}}{2} = V_{AB} - V_{AA} + V_{AA} - \frac{V_{AA} + V_{BB}}{2}, \tag{1.39}$$

which results in:

$$V_{AB} - V_{AA} = V - \frac{V_{AA} - V_{BB}}{2}. \tag{1.40}$$

Similarly, $V_{AB} - V_{BB}$ can be calculated, which equals:

$$V_{AB} - V_{BB} = V + \frac{V_{AA} - V_{BB}}{2}. \tag{1.41}$$

This makes the system simpler, because both equations contain the term $(V_{AA} - V_{BB})$. Due to this fact, one can describe the same system with two parameters (M and V) instead of three (V_{AA}, V_{AB}, V_{BB}), where M:

$$M = \frac{V_{AA} - V_{BB}}{2}. \tag{1.42}$$

By modifying equation (1.40) and (1.41) the following expressions occur:

$$\begin{aligned} V_{AB} - V_{AA} &= V - M \\ V_{AB} - V_{BB} &= V + M. \end{aligned} \tag{1.43}$$

Out of these two energy parameters, V determines the chemical properties of the system. In order to make it more understandable, two additional parameters are being introduced (α_i and ε_i):

$$\alpha_i = [Z_v(c_{i-1} + c_i + c_{i+1} + c_{i+2}) + Z_l(c_i + c_{i+1})]M \tag{1.44}$$

$$\varepsilon_i = [Z_v(c_{i-1} + c_{i+1} - c_i - c_{i+2}) + Z_l(c_i - c_{i+1})]V \tag{1.45}$$

Both of these parameters depend on four concentrations: the two planes where the jump takes place (c_i, c_{i+1}) and the closest neighbouring planes (c_{i-1}, c_{i+2}). $E_{i,i+1}$ can be transformed into:

$$E_{i,i+1} = \hat{E^0} - \alpha_i + \varepsilon_i, \tag{1.46}$$

where $\hat{E^0}$ contains all the terms that do not depend on the concentration. It can be shown, that the activation energy of a backward jump is:

$$E_{i+1,i} = \hat{E^0} - \alpha_i - \varepsilon_i. \tag{1.47}$$

$\Gamma_{i,i+1}$ can be written in a much simpler form:

$$\Gamma_{i,i+1} = \nu \ \exp\left(-\frac{\hat{E^0} - \alpha_i + \varepsilon_i}{k_B T}\right) = \Gamma_0 \ \exp\left(\frac{\alpha_i - \varepsilon_i}{k_B T}\right), \tag{1.48}$$

where $\Gamma_0 = \nu \ \exp(-\frac{\hat{E^0}}{k_B T})$. Based on these $\Gamma_{i+1,i}$ can be written as:

$$\Gamma_{i+1,i} = \Gamma_0 \ \exp\left(\frac{\alpha_i + \varepsilon_i}{k_B T}\right). \tag{1.49}$$

Applying this on the detailed balance condition results exactly $\tilde{\mu}_i = \tilde{\mu}_{i+1}$, i.e. this choice of Γ satisfies the requirements.

The physical meaning of M and α_i can be explained by taking a homogenous system: $c_i = c \ \forall \ i$. In this case the value of α_i is:

$$\alpha_i = (4Z_v c + 2Z_l c)M = 2ZMc \tag{1.50}$$

and ε_i is zero. In this extreme case:

$$\Gamma(c) = \Gamma_0 \exp\left(\frac{2ZM}{k_B T} c\right). \tag{1.51}$$

One can see the form of the exponentially dependent difussion coefficient ($D = D_0 \ \exp(mc)$): $m = 2ZM/kT$. If we introduce m', the results are given in order of magnitude:

$$m' = m \lg e. \tag{1.52}$$

Connecting m' and m, the following expression comes up:

$$m' = \frac{2ZM}{k_B T} \lg e. \tag{1.53}$$

This parameter can be estimated from experiments, because this is the strength of the diffusion coefficient's dependence on the concentration. Con-

sequently, α_i represents the concentration dependence of the tracer diffusion coefficient and ε_i contains the thermodynamic factor.

It must be noted, that this is not the only choice of Γ which fulfills the conditions. Another example can be found in the so called *Kinetic Tight-Binding Ising Model* (KTBIM) [13]. The difference between the two choices is that the KTBIM only contains ε_i and α_i is not present, although it still fulfills the conditions.

A simulation starts with an initial configuration (concentration distribution), α_i and ε_i must be calculated, where M and V are input parameters. The value of Γ can be determined, which makes it possible to calculate the atomic fluxes. These steps are repeated over and over again. One could say that this is a relatively simple but effective method.

Stochastic kinetic mean-field

The SKMF approach [14, 15] [1] is based on the model of Martin [11]. Here, the local atomic configuration in an A-B binary alloy is described by the occupation probability c_i of A atoms on a site i, so that $1 - c_i$ is the occupation probability of B atoms on the same site. The time evolution of c_i is governed by a non-linear stochastic equation satisfying the balance of the conservation of matter and the fluxes of atoms between the site i and its Z nearest neighbouring sites j:

$$\frac{\mathrm{d}c_i}{\mathrm{d}t} = \sum_{j=1}^{Z} \left[J_{j,i} - J_{i,j} \right] . \tag{1.54}$$

In this equation, $J_{j,i}$ and $J_{i,j}$ are the material fluxes of A atoms from site j to site i and vice versa, both containing a mean-field and a fluctuation part:

[1] This section is based on the result of the article *Stochastic kinetic mean field model* [14, 15]. I am a co-author of this paper, however it was already accepted as a work of János J. Tomán in his PhD thesis.

$$J_{i,j} = J_{i,j}^{\mathrm{MF}} + \delta J_{i,j}^{\mathrm{Lang}}. \tag{1.55}$$

Here, $J_{i,j}^{\mathrm{MF}}$ is the mean-field (MF) atomic flux from site i to site j, defined from the mean-field (MF) exchange rate $\Gamma_{i,j}^{\mathrm{MF}}$ between sites i and j as follows:

$$J_{i,j}^{\mathrm{MF}} = c_i(1-c_j)\Gamma_{i,j}^{\mathrm{MF}}. \tag{1.56}$$

Similarly, the fluctuation part $\delta J_{i,j}^{\mathrm{Lang}}$ in the total flux can be expressed from a dynamic Langevin noise $\delta_{i,j}^{\mathrm{Lang}}$ as [14]:

$$J_{i,j}^{\mathrm{Lang}} = c_i(1-c_j)\delta_{i,j}^{\mathrm{Lang}}, \tag{1.57}$$

where the dynamic Langevin noise $\delta_{i,j}^{\mathrm{Lang}}$ is a white noise of amplitude A_n:

$$\delta_{i,j}^{\mathrm{Lang}} = \frac{A_n}{\sqrt{\mathrm{d}t}}\theta. \tag{1.58}$$

In compliance with the definition of a Gaussian noise, θ is a random uniform number of zero mean value and a mean squared value equal to 1. The introduction of stochasticity in the SKMF model makes it possible to describe the initial stages of nucleations, thereby overcoming one limitation of the deterministic model of Martin. It should be noted that adding the noise to the flux rather than the concentration notably allows to circumvent potential singularities in the composition change rates [14]. When A_n is set to zero, the SKMF model becomes purely deterministic.

The MF jump frequency $\Gamma_{i,j}^{\mathrm{MF}}$ is defined as:

$$\Gamma_{i,j}^{\mathrm{MF}} = \nu \exp\left(-\frac{E_0 - (E_i^A + E_j^B)}{k_B T}\right). \tag{1.59}$$

Each energy E_s^X ($X = A, B$, $s = i, j$) is the sum of the interaction energies between an atom X on site s and the atoms on the Z nearest neighbour sites in the first coordination shell:

$$E_s^X = \sum_{l=1}^{Z} \left[c_l V_{AX} + (1 - c_l) V_{XB} \right]. \tag{1.60}$$

Now, an equivalent expression of the MF jump frequency $\Gamma_{i,j}^{\mathrm{MF}}$ is used in practice in SKMF simulations, on introducing the parameters:

$$M = \frac{1}{2}(2V_{AA} - V_{BB}), \quad V = \frac{1}{2}(V_{AB} - [V_{AA} + V_{BB}]). \tag{1.61}$$

In this expression, the parameter V corresponds to the mixing energy of the solid solution, and the parameter M accounts for the A/B asymmetry of the interdiffusion coefficient. Then, $\Gamma_{i,j}^{\mathrm{MF}}$ can customarily be rewritten in the alternative form:

$$\Gamma_{i,j}^{\mathrm{MF}} = \Gamma_0 \exp\left(-\frac{\hat{E}_{i,j}}{k_B T} \right), \tag{1.62}$$

where $\Gamma_0 = \nu \exp\{[-E_0 + Z(V_{AB} + V_{BB})]/k_B T\}$, and $\hat{E}_{i,j}$ is an effective interaction energy defined by:

$$\hat{E}_{i,j} = (M - V) \sum_{\substack{l=1, \\ l \in \mathcal{V}(i)}}^{Z} c_l + (M + V) \sum_{\substack{l=1, \\ l \in \mathcal{V}(j)}}^{Z} c_l. \tag{1.63}$$

The summation spans sites in the vicinity $\mathcal{V}(i)$ of site i and in the vicinity $\mathcal{V}(j)$ of site j in the first and second term respectively.

To connect the atomistic parameters defining the MF jump frequency in formula (1.59) to the sought expression of the Mean-Field Bragg-Williams free energy, the internal energy u_i of a site i can first be calculated from the mean interaction energy of this atom with the first coordination shell:

$$u_i = \frac{1}{2} \left(c_i E_i^A + (1 - c_i) E_i^B \right). \tag{1.64}$$

Here, the factor $1/2$ compensates the double counting of interactions. Using expression (1.60) for the energies E_i^A and E_j^B, and expression 1.61 for the parameters M and V, the mean internal energies can be rewritten as:

$$\begin{aligned} u_i = & f_A c_i + f_B(1-c_i) + c_i(1-c_i)V_0 \\ & + \frac{1}{2}(\bar{c}_l - c_i)\left[ZM + (1-2c_i)V_0\right], \end{aligned} \tag{1.65}$$

where $f_A = ZV_{AA}/2$, $f_B = ZV_{BB}/2$, $V_0 = ZV$, and $\bar{c}_l = 1/Z\sum_{l=1}^{Z} c_l$ is the local average concentration of A atoms in the vicinity of the site i.

In a homogeneous binary solution, the probability c_i to find an atom A in site i and the locally averaged probability $\bar{c}_l$ reduce to the average concentration c of the alloy: $c_i = \bar{c}_l \equiv c$. Accordingly, the internal energy u_i of an atom A on site i is equal to the density of internal energy u in the homogeneous solution: $u_i \equiv u(c) = f_A c + f_B(1-c) + c(1-c)V_0$. Moreover, the density of entropy reads $s(c) = k_B\left[c\ln c + (1-c)\ln(1-c)\right]$. Thus, the regular solid solution model for the free energy per atom $f_h(c) = u(c) - Ts(c)$ is recovered for the homogeneous solution:

$$\begin{aligned} f_0(c) = & f_A c + f_B(1-c) + c(1-c)V_0 \\ & + k_B T\left[c\ln c + (1-c)\ln(1-c)\right]. \end{aligned} \tag{1.66}$$

As can be seen, the first two terms are the internal energies of the pure A and B components, and the excess free energy density is the MFBW free energy:

$$\Delta f_0 = c(1-c)V_0 + k_B T\left[c\ln c + (1-c)\ln(1-c)\right]. \tag{1.67}$$

Obviously, Δf_0 is symmetrical, so that only symmetrical solubility limits corresponding to the minima of Δf_0 can be accounted for at equilibrium. Consequently, the stationary states of the original SKMF model [14] could only display symmetrical solubility limits as well. The model and the computer simulation technique can be used in a wide variety of applications.

The typical length- and timescales that can be simulated with the method conveniety fits next to the already available methods, as visualized on 1.4.

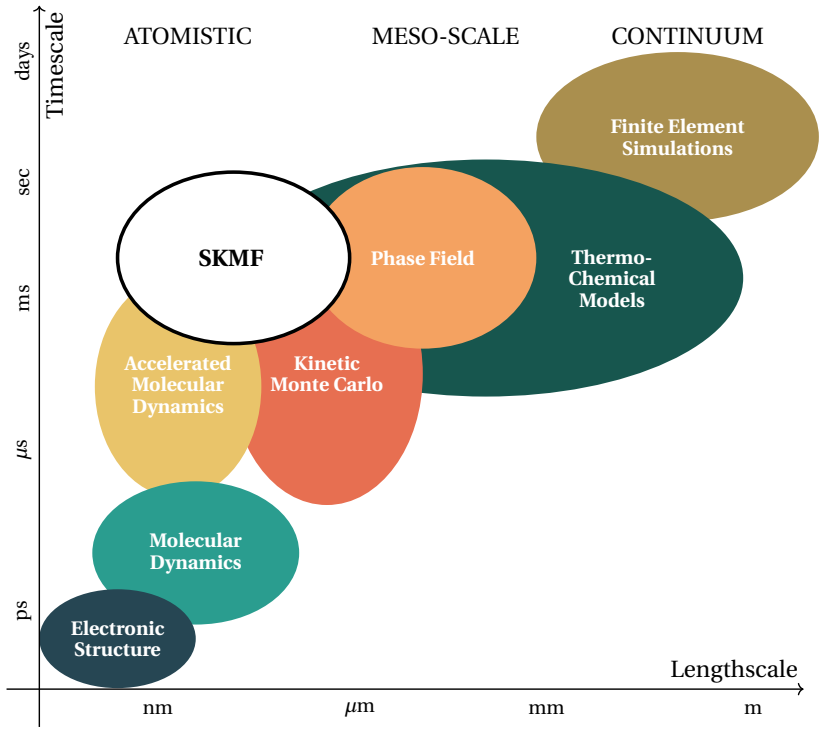

Figure 1.4: Typical time and length scales of different computer simulation techniques. Figure is based on [16], but with the addition of SKMF.

Chapter 2

Composition dependent gradient energy coefficient

In this chapter, the kinetics of the phase transformation in the silver-copper system is being investigated. The results of the atomistic computer simulations and the analytical calculations are presented in the following sections. [1]

The applied numerical approach, the SKMF model, has already been presented in the previous chapter, which is suitable for the study of solid state atomic motion processes in multicomponent systems [14, 15, 18]. It should be mentioned, however, that not only the original SKMF model was used in this chapter, but an improved version of it, as the method originally published only allowed the study of regular solids solutions with symmetric spinodal curves and solubility limits. Additional regular solid solution parameter was introduced into the approach and the equations used were modified accordingly. This makes the model able to investigate non-regular solid solutions, for which the solubility curves are asymmetric,

[1] The chapter is based on the article B. Gajdics et al. Composition dependent gradient energy coefficient: How the asymmetric miscibility gap affects spinodal decomposition in Ag-Cu? *Calphad*, 67:101665, 2019. [17]

as in the case of the silver-copper two-component system.

The field of application of Ag-Cu is diverse as it provides advantageous physical and chemical properties. Its excellent mechanical strength is coupled with its high conductivity and thus it has applications in electrical interconnection technologies, microstructure patterning [10], in the field of catalysis [19, 20] and in the production of two-component alloy nanoparticles [21] and for a new generation of brazing materials for Inconel® 718 [22]. Thanks to its wide miscibility gap, it is also excellent as a model system.

The silver-copper two-component system is an eutectic alloy in which the Ag- and Cu-rich phases can be in equilibrium with the liquid phase. Both of these solid phases have fcc crystal structure and below the critical temperature, the free energy of the system can be described by a two minimum function that connects the two phases. A heterogeneous spatial pattern is formed during diffusion processes that changes the electrical and mechanical state of the system. In order for the system to be properly designed for use, an in-depth knowledge of the kinetics of this phase separation mechanism is required.

In the case of the Ag-Cu system, we assume the homogeneous free energy density as [21, 23]:

$$\begin{aligned} f_0 = {} & f_{Ag}c + f_{Cu}(1-c) \\ & + c(1-c)\left[V_0 + V_1(2c-1)\right] \\ & + k_B T[c\ln(c) + (1-c)\ln(1-c)], \end{aligned} \tag{2.1}$$

where c is the Ag tomic fraction, T is the absolute temperature, k_B is the Boltzmann constant, $f_{Ag} = \tilde{f}_{Ag}/N_A$, $f_{Cu} = \tilde{f}_{Cu}/N_A$, $V_0 = \tilde{V}_0/N_A$, $V_1 = \tilde{V}_1/N_A$ where N_A is the Avogadro constant and $\tilde{f}_{Ag} = -11945 + 9.67T$ J/mol, $\tilde{f}_{Cu} = -13054 + 9.62T$ J/mol, $\tilde{V}_0 = 34532 - 9.178T$ J/mol, $\tilde{V}_1 = -5996 + 1.725T$ J/mol. In practice, the first two terms in the equation correspond to the internal and free energies of the pure A and B components. The excess free energy due to phase transformation and mixing is therefore:

$$\begin{aligned}\Delta f_{ex} = c(1-c)\,[V_0 + V_1(2c-1)] \\ + k_B T[c\ln(c) + (1-c)\ln(1-c)].\end{aligned} \tag{2.2}$$

This relationship was plotted in Fig. 2.1 as a function of the concentration c of the Ag component at $T = 873$ K. The coefficients V_0 and V_1 were chosen in such a way that they could be used to adequately describe the two-component system [24], especially bearing in mind that the asymmetric appearance of the f_0 function was determined on the basis of experimental phase diagram results.

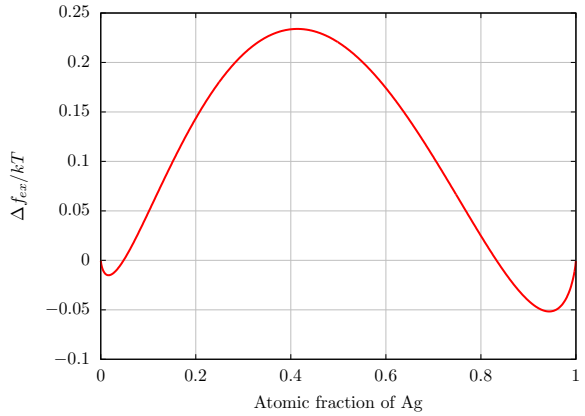

Figure 2.1: $\Delta f_{ex}(c)$ excess free energy density function calculated from Eq. (2.2) at $T = 873$ K for the Ag-Cu system.

2.1 Free energy

In section 1.2.2, it has been shown that SKMF in its original form is only suitable for modeling regular solid solutions because its excess free energy curve is symmetric, and leads to symmetric spinodal curve and miscibility gap.

The formula $F = U - TS$ was taken to calculate the free energy, where

U is the internal energy and S stands for the entropy. If we want to evaluate the internal energy of a system in a three-dimensional model like SKMF, it is necessary to know the interaction energies between the atoms:

$$U = \frac{1}{2}\sum_{i=1}^{N} \overline{V}_i = \sum_{i=1}^{N} u_i, \tag{2.3}$$

where N is the total number of sites in the system. In Eq. 2.3, $\overline{V}_i$ gives the mean interaction energy on site i for one atom; dividing by two serves to take each pair into account only once and the mean internal energy on site i is $u_i = \overline{V}_i/2$.

The calculation of the mean interaction energy on site i is determined by the interaction energy of the atom A at site i weighted by its finding probability and the interaction energy of the atom B on the same site weighted by its own finding probability on site i. Note that the combined probability of finding A or B atoms at a given i site is 1, since c_i is the probability of finding A and $1 - c_i$ of finding B atoms.

$$\overline{V}_i = c_i E_i^A + (1 - c_i) E_i^B. \tag{2.4}$$

Each $\overline{V}_i$ term used to calculate the internal energy of the system, corresponds to the interaction energies in the activation energy used in the SKMF model.

By applying Eqs. (1.60), (2.3) and (1.64), the free energy density of the system is given as:

$$\begin{aligned} u_i = &\frac{1}{2} Z c_i V_{AA} + \frac{1}{2} Z (1 - c_i) V_{BB} + Z c_i (1 - c_i) V \\ &+ \frac{1}{2} Z (\bar{c}_l - c_i) \left[\frac{V_{AA} - V_{BB}}{2} + (1 - 2c_i) V \right]. \end{aligned} \tag{2.5}$$

where:

$$\bar{c}_l = \frac{1}{Z}\sum_{l=1}^{Z} c_l. \tag{2.6}$$

Eq. (2.5) can be reformulated for the sake of clarity as:

$$\begin{aligned} u_i = {} & u_A c_i + u_B(1-c_i) + c_i(1-c_i)V_0 \\ & + \frac{1}{2}(\bar{c}_l - c_i)\left[ZM + (1-2c_i)V_0\right] \end{aligned} \tag{2.7}$$

with $u_A = ZV_{AA}/2$, $u_B = ZV_{BB}/2$ and $V_0 = ZV$.

If one takes a homogeneous binary solution into account, $c_i = \bar{c}_l \equiv c$, and:

$$u_i \equiv u = u_A c + u_B(1-c) + c(1-c)V_0. \tag{2.8}$$

In the case of a homogeneous solution $U = Nu$ (see Eq. (2.3)) is the internal energy, and its entropy is given as $S = Ns = -Nk_B\left[c\ln c + (1-c)\ln(1-c)\right]$. Thus, for a homogeneous solid solution, the free energy per atom can be calculated as:

$$\begin{aligned} f_0^{\mathrm{SKMF}} = {} & u_A c + u_B(1-c) + c(1-c)V_0 \\ & + k_B T\left[c\ln c + (1-c)\ln(1-c)\right]. \end{aligned} \tag{2.9}$$

However, it contains the internal and free energy terms for the pure A and B component (the first and second term), i.e. in the solid solution model this is the homogeneous free energy per atom. We can take the excess free energy density from the equation:

$$\begin{aligned} \Delta f_{ex}^{\mathrm{SKMF}} = {} & c(1-c)V_0 \\ & + k_B T\left[c\ln c + (1-c)\ln(1-c)\right]. \end{aligned} \tag{2.10}$$

In the SKMF model, in its original form, the excess free energy density function is symmetrical to $c = 0.5$ as it can be seen on Fig. 2.2. This is

due to the fact that the relationships determining the thermodynamics of the SKMF approach are based on a regular solid solution model. Consequently, systems with asymmetric miscibility gap and spinodal curve cannot be studied with the model in this form. If, however, one inspects Eq. (1.67) and Eq. (2.2), can see that in case of $V_0 = ZV$ (V_0 is for one atom, V is for one bond) they differ by the first terms.

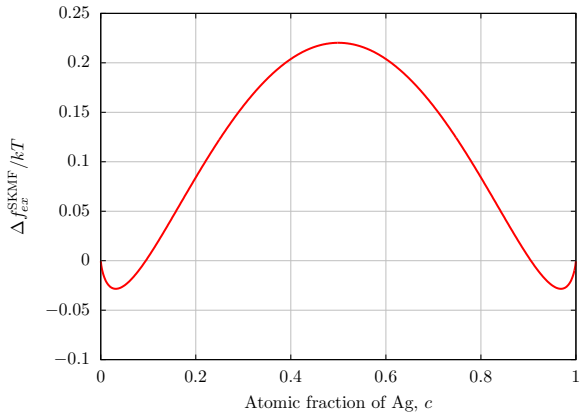

Figure 2.2: Using Eq. (1.67), the excess free energy density was calculated for the Ag-Cu system as in the original SKMF model, at $T = 873$ K.

2.2 Improvement of SKMF

In order to be able to make a more realistic description of the system, thus getting closer to the experimentally observed phase diagram, we made modifications to the original SKMF model. This means that it is necessary to choose the free energy density such as in Eq. (2.1). From this we can assume that in the equation Eq. (1.65) instead of a constant V_0, a composition dependent interaction energy parameter should be selected:

$$V(c_{ij}) = V_0 + V_1(2c_{ij} - 1). \tag{2.11}$$

The term c_{ij} was defined as:

$$c_{ij} = \frac{c_i + \sum_{l=1}^{Z} c_l + c_j + \sum_{n=1}^{Z} c_n}{2(Z+1)}. \tag{2.12}$$

However, it is important to note here that it would be possible to introduce the parameter $V(c)$ not only by assuming a linear dependence, but also other arbitrarily chosen functions could be implemented. One such function is the Redlich-Kister polynomial [2], which is widely used in CALPHAD [25]:

$$V(c) = \sum_{v=0}^{n} V_v (2c-1)^v. \tag{2.13}$$

This would of course be achieved in the case of the SKMF model by applying the term c_{ij} instead of c in the equation. The V_v parameters are usually determined phenomenologically by fitting phase equilibrium and thermodynamic data. However, there are also other works where they are taken from ab initio calculations [26–28]. The value of n sets whether a given solution will be regular or sub-regular. In the case of $n = 0$ the solution is regular, while $n = 1$ corresponds to the sub-regular region and the value of n is typically less than or equal to 2.

We have prepared an open-source implementation of the method [14, 15] and this version can be found on the website http://skmf.eu. In addition, we have made available a code that includes the modifications presented here, such as the $V(c)$ composition-dependent interaction energy coefficient in Eq. (2.11).

The program also requires an input file, which can be found on the same the website. It includes all the parameters of the simulation which must be specified, such as: the crystal structure of the sample, which determines the coordination number Z; the required energy parameters, which are M, V_0 and V_1 respectively for the improved method instead of M and V as in

the original SKMF model. The T absolute temperature parameter is also necessary to perform simulations. The inputs listed here are sufficient to describe the kinetics and thermodynamics of the system. A brief summary of the solution algorithm is being presented in the followings.

Basically, the first two terms are responsible for the outgoing and incoming atomic fluxes of the A component. It should be noted, however, that the outgoing atomic flux of a lattice site corresponds to the incoming flux of an adjacent lattice site. In order not to calculate these terms unnecessarily twice, only the output fluxes are computed. The equations (1.62), (1.63), (2.11) and (2.12) are used for the solution of Eqs. (1.56) and they are used in their dimensionless form. For this we introduce dimensionless time $\tau \equiv \Gamma_0 t$ and dimensionless flux $\widetilde{J}_{i,j} \equiv J_{i,j}/\Gamma_0$. After calculating the fluxes, multiplying them by a small, finite dimensionless timestep we receive how the composition profile will evolve in the system during that time.

These calculations were performed in the deterministic limit of the SKMF model, which is a highly simplified version of it. The description of the general case can be found in the previous chapter and in [14].

2.3 Results and discussion

Gradient energy coefficient

In this section, I show that the SKMF model inherently contains the gradient energy coefficient. It is not an input parameter of the simulations. This approach, in its original form contains a κ which corresponds exactly to the Eq. (1.8) form and this will be shown as well for the regular solution case, where $V_1 = 0$ and the the miscibility gap is symmetric. Furthermore, this equation can be written in a general form, which includes the composition dependent V interaction energy as in Eq. (2.13) and a composition dependent κ as well.

First of all, $\vec{r}_i$ and $\vec{r}_l$ is being introduced for the sake of convinience,

where these are the radius vectors of the i and l sites, as well as $c_i = c(\vec{r}_i)$ and $c_l = c(\vec{r}_l)$ can be used to reformulate Eq. (1.65) as:

$$\begin{aligned} u(c(\vec{r}_i)) = u_A c(\vec{r}_i) + u_B(1 - c(\vec{r}_i)) \\ + c(\vec{r}_i)(1 - c(\vec{r}_i))V_0 + \frac{1}{2}(\bar{c}(\vec{r}_l) - c(\vec{r}_i)) \\ \cdot [ZM + (1 - 2c(\vec{r}_i))V_0]\,. \end{aligned} \tag{2.14}$$

Cahn and Hilliard introduced $\vec{r}_0 = \vec{r}_l - \vec{r}_i$ which is the radius vector of the site l relative to site i. [1] Using this vector, one can write c_l as a function of c_i as follows:

$$c(\vec{r}_l) = c(\vec{r}_i) + \vec{r}_0 \nabla c(\vec{r}_i) + \frac{1}{2}(\vec{r}_0 \nabla)^2 c(\vec{r}_i) + \ldots . \tag{2.15}$$

Using this expression (neglecting the third and higher derivatives) we can calculate $\bar{c}(\vec{r}_l) - c(\vec{r}_i)$. By expressing Eq. (2.15) in terms of vector components and performing the summation indicated in Eq. (2.6) we obtain for a cubic lattice:

$$\bar{c}(\vec{r}_l) - c(\vec{r}_i) = \frac{1}{6} r_0^2 \nabla^2 c(\vec{r}_i). \tag{2.16}$$

Substituting this expression into Eq. (2.14), we obtain the internal energy per atom of an inhomogeneous solution:

$$\begin{aligned} u = u_A c + u_B(1 - c) + c(1 - c)V_0 \\ + \frac{1}{12} r_0^2 \left[ZM + (1 - 2c)V_0\right] \nabla^2 c. \end{aligned} \tag{2.17}$$

Considering that the free energy per atom for an inhomogeneous solution is $f = u - Ts = f_0(c) + \kappa_1 \nabla^2 c + \kappa_2 (\nabla c)^2$ (see Eq. (1.1)), we can find:

$$
\begin{aligned}
f_0 &= u_A c + u_B(1-c) + Zc(1-c)V_0 \\
&\quad + kT\left[c\ln c + (1-c)\ln(1-c)\right], \\
\kappa_1 &= \frac{1}{12} r_0^2 \left[ZM + (1-2c)V_0\right], \\
\kappa_2 &= 0.
\end{aligned}
\tag{2.18}
$$

Applying now Eq. (1.5), we obtain:

$$
\kappa = \frac{r_0^2 V_0}{6}, \tag{2.19}
$$

which is equivalent to κ_R given by Eq. (1.8) as $r_0^2/3 = \xi^2$.

To generalise this expression, only V_0 has to be replaced by a composition dependent interaction parameter in Eq. (2.14) and consequently also in Eq. (2.18). Thus

$$
\kappa(c) = -\frac{1}{12} r_0^2 \frac{\partial (1-2c)V(c)}{\partial c}. \tag{2.20}
$$

Substituting for instance $V(c)$ given in Eq. (2.13) into Eq. (2.20) results in:

$$
\kappa(c) = \frac{1}{6} r_0^2 \sum_{v=0}^{n} (1+v) V_v (2c-1)^v. \tag{2.21}
$$

This gives back Eq. (2.19) for $n = 0$ (regular solution) and results in a linearly composition dependent gradient energy coefficient for $n = 1$ (sub-regular solution):

$$
\kappa(c) = \frac{1}{6} r_0^2 \left[V_0 + 2V_1(2c-1)\right]. \tag{2.22}
$$

At the end of this section, it should be emphasized that in the case, when composition dependent $V(c)$ interaction energy is used in the system, it necessarily implies that the κ gradient energy coefficient will also be composition dependent. Thus, for systems with an asymmetric solubility curve, the use of a composition dependent gradient energy coefficient is

also required when performing computer model calculations. However, we often come across authors who do not take this fact into account in their simulations.

Miscibility gap

Tests were performed on how well the solubility data obtained from SKMF fit the miscibility gap calculated from the free energy function Eq. (2.1) using the common tangent method. The results are virtually identical in these two cases. First, the case of the regular solid solution was investigated, where the V_1 interaction energy coefficient is set to zero. The corresponding results can be seen in Fig. 2.3a and they show an excellent match. I performed the same test for the case where V_1 is not equal to zero, i.e. for a non-regular solid solution, but the calculation was made by using the improved verion of the model. As it was expected, the miscibility gap becomes indeed somewhat asymmetric, as can be seen in Fig. 2.3b, and the solubility data obtained here show a good agreement with the data obtained from the free energy function. This shows, that the improved SKMF model can indeed reproduce the Ag-Cu like miscibility curves.

Note that to calculate the f_0^L free energy per atom of the liquid phase, similarly to Eq. (2.1), the following formula was used:

$$\begin{aligned} f_0^L = & f_{Ag}^L c + f_{Cu}^L (1-c) \\ & + c(1-c)\left[L_0 + L_1(2c-1)\right] \\ & + kT[c\ln(c) + (1-c)\ln(1-c)]. \end{aligned} \tag{2.23}$$

Here $f_{Ag}^L = \tilde{f}_{Ag}^L/N_A$, $f_{Cu}^L = \tilde{f}_{Cu}^L/N_A$, $L_0 = \tilde{L}_0/N_A$, $L_1 = \tilde{L}_1/N_A$, where $\tilde{f}_{Ag}^L = 0$, $\tilde{f}_{Cu}^L = 0$, $\tilde{L}_0 = 15171 - 2.537T$ J/mol and $\tilde{L}_1 = -2425 + 0.946T$ J/mol are the thermodynamic parameters of the Ag-Cu liquid phase. In the $V_1 = 0$ case $L_1 = 0$ and $f_{Cu}^L = f_{Ag}^L$ parameters were chosen in order to obtain a symmetric phase diagram.

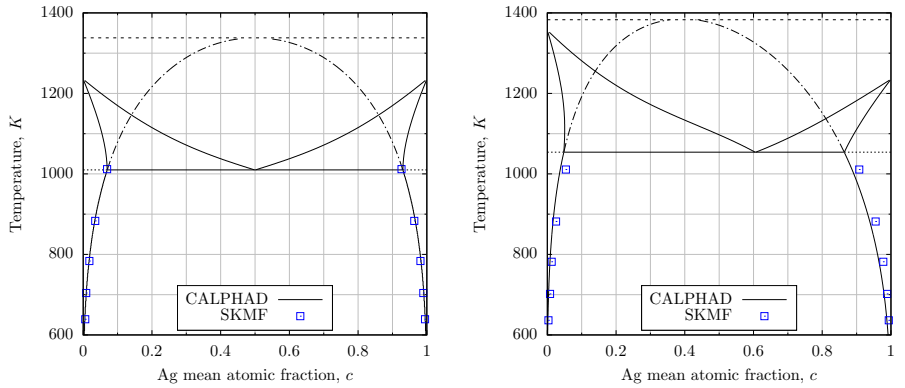

(a) Miscibility curves, $V_1 = 0$ (b) Miscibility curves, $V_1 \neq 0$

Figure 2.3: Calculated miscibility gaps provided by SKMF: (a) $V_1 = 0$ and (b) $V_1 \neq 0$.

Interface profile

The interfacial free energy density can be expressed as [1]:

$$\sigma = \rho \int_{-\infty}^{+\infty} \left[\Delta f(c) + \kappa(\nabla c)^2\right] \mathrm{d}x, \tag{2.24}$$

where

$$\Delta f(c) = f_0 - \left[c\mu_A^{eq} + (1-c)\mu_B^{eq}\right] \tag{2.25}$$

and μ_A^{eq} and μ_B^{eq} are the chemical potentials per atom of A and B in the α and β phases, respectively.

The equilibrium composition profile can be obtained by minimizing Eq. (2.24). By applying the appropriate Euler-Lagrange equation for the composition field, we obtain [4]:

$$\kappa(\nabla c)^2 = \Delta f(c) \tag{2.26}$$

The following formula can be obtained for the quilibrium interface by sep-

arating the variables and calculating the integral:

$$x(c) = \int \sqrt{\frac{\kappa(c)}{\Delta f(c)}} \mathrm{d}c. \tag{2.27}$$

To obtain the composition profile, we first calculated the μ_A^{eq} and μ_B^{eq} from the free energy per atom expression, then calculated $\Delta f(c)$ form Eq. (2.25), and calculated the integral numerically. Finally, we inverted the $x(c)$ function.

Figure 2.4 shows the calculated interface profiles compared to equilibrium composition profiles obtained by SKMF for composition independent and linearly composition dependent gradient energy coefficients. To obtain the equilibrium composition profiles in SKMF, an A/B diffusion pair was created initially in the computational cell and the program run for very long time, until no change was seen in the composition profile (also in the free energy). As can be seen, the agreement between the corresponding profiles is excellent. The minor deviation comes from that the theoretical solubilities slightly differ from that obtained from SKMF (see Fig. 2.3).

Figure 2.5 shows the comparison of the theoretical interface profiles presented in Fig. 2.4. As can be seen the slope and the width of the interfaces hardly differ with the parameters of the Ag-Cu system. The most remarkable difference is that in the case of a composition dependent gradient energy coefficient the interface is asymmetric due to the asymmetry in the solubility of Cu in Ag and vice versa.

Note that in SKMF we used zero noise amplitude ($A_n = 0$) for the calculation, which means that the calculation was free from stochastic fluctuations. We also tested the interface profiles with high stochastic fluctuations (up to $A_n = 0.3\sqrt{\Gamma_0}$), but they practically did not change.

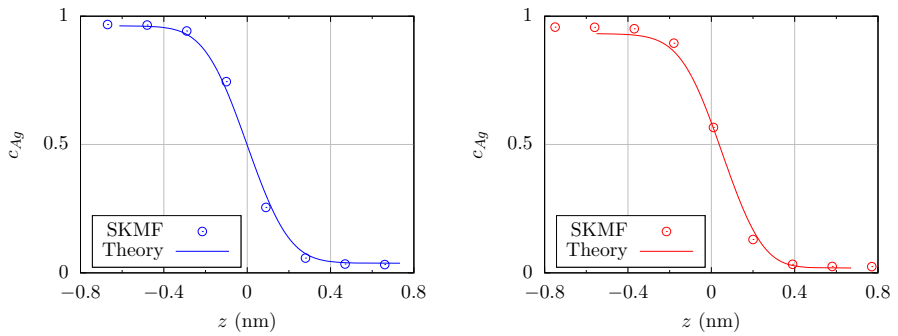

(a) Interface profile, $V_1 = 0$

(b) Interface profile, $V_1 \neq 0$

Figure 2.4: Theoretical interface profiles calculated by using Eq. (2.27) compared to the equilibrium composition profiles obtained by SKMF: (a) $V_1 = 0$ (regular solution, symmetric miscibility gap), i.e. composition independent κ_R; (b) $V_1 \neq 0$ (non-regular solution, asymmetric miscibility gap), i.e. linearly composition dependent $\kappa_R(c)$.

Spinodal decomposition

We first performed the calculations with its original form (regular solid solution) and then repeated with the improved one (non-regular solution). For $\bar{c} = 0.3$, the evolution of the concentration field of silver is displayed in Fig. 2.6.

The time evolution of the λ_c cutoff wavelength, and the fastest growing wavelength λ_m was investigated, which is - based on the classical Cahn-Hilliard theory - in a relationship with λ_c as $\lambda_m = \sqrt{2}\lambda_c$ [21] In the SKMF simulations, the average Ag composition is $\bar{c}$ and the structure factor was calculated as [29] $S(k,t) =< \hat{c}(\boldsymbol{k},t)\overline{\hat{c}(\boldsymbol{k},t)} >$. The $\hat{c}(\boldsymbol{k},t)$ and $\overline{\hat{c}(\boldsymbol{k},t)}$ terms are the Fourier transform and complex conjugate of $c(\boldsymbol{r},t)$ at t. $k = |\boldsymbol{k}|$ is the radially averaged wave vector, and $< \cdot >$ is the average over initial configurations. In the Cahn-Hilliard linear theory [30], only the composition fluctuations with spatial extension exceeding the reduced cutoff wavelength λ_c can trigger the phase separation. Here, λ_c is approximated by $2\pi/k_c$,

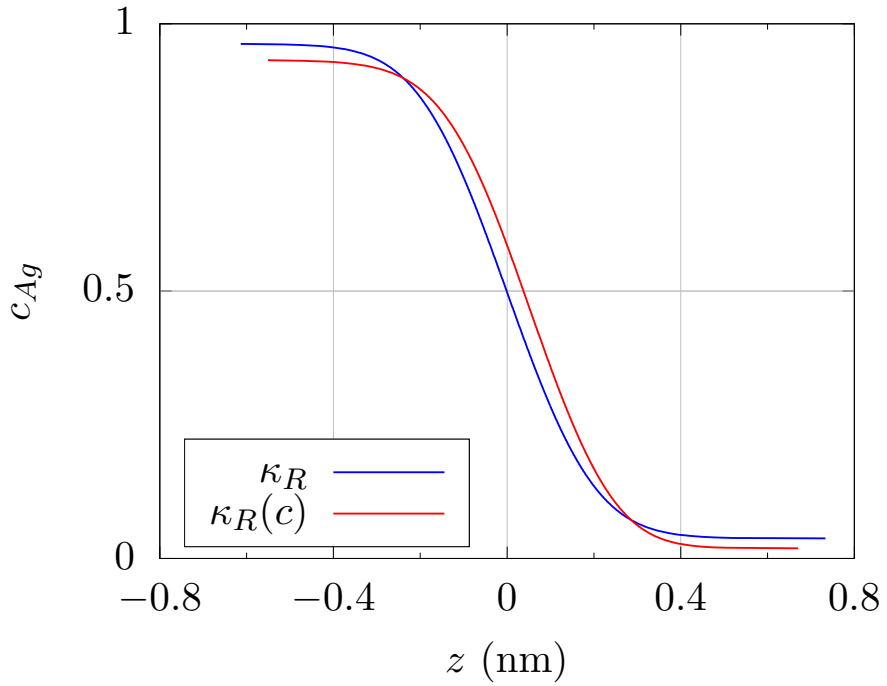

Figure 2.5: Comparison of the theoretical interface profiles calculated by using Eq. (2.27) (see Fig. 2.4).

where k_c is the maximum wave vector whose amplitude $S(k_c, t)$ exponentially increases during the early stage of the spinodal decomposition (see Fig. 2.7a). As for the reduced maximum wavelength λ_m, it corresponds to the fastest growing wavelength. Thus, it can be approximated by $2\pi/k_m$, where k_m is the wave vector corresponding to the maximum value of $S(k, t)$ (see Fig. 2.7b).

The values of λ_c and λ_m were determined as a function of the $\bar{c}$ mean composition. The results of the SKMF simulations are shown in Fig. 2.8, and they were performed at $T = 873$ K temperature for the $V_1 = 0$ regular solution and $V_1 \neq 0$ non-regular solution cases. Here, too, symmetric and asymmetric behaviour can be observed compared to $c_{Ag} = 0.5$ respectively.

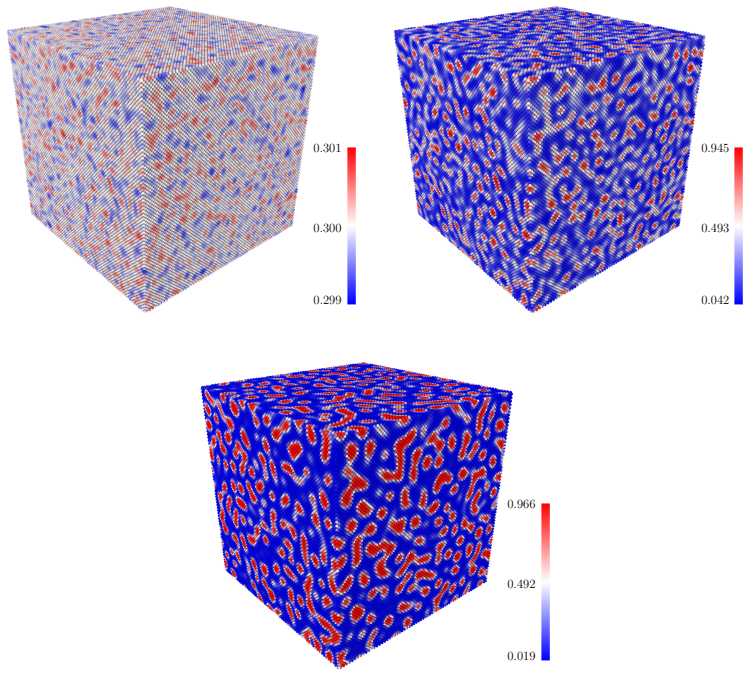

Figure 2.6: Three-dimensional visualization of several time steps of an SKMF simulation showing a phase separating silver-copper system. At the beginning of the run, a homogenous $\bar{c} = 0.3$ average composition was taken with a small static fluctuation (0.002), at $T = 873$ K temperature.

In the case of spinodal decomposition, examining a two-component system, it was also shown analytically [21] that the dependence of the cutoff and critical wavelength on the composition can also be estimated. Using the classical Cahn-Hilliard theory λ_c can be expressed as:

$$\lambda_c = \sqrt{\frac{-8\kappa_R\pi^2}{f_0''}}. \tag{2.28}$$

Here f_0'' is the second derivative of the f_0 free energy function by composition. This f_0'' derivative can be substituted into Eq. (2.28) which gives us:

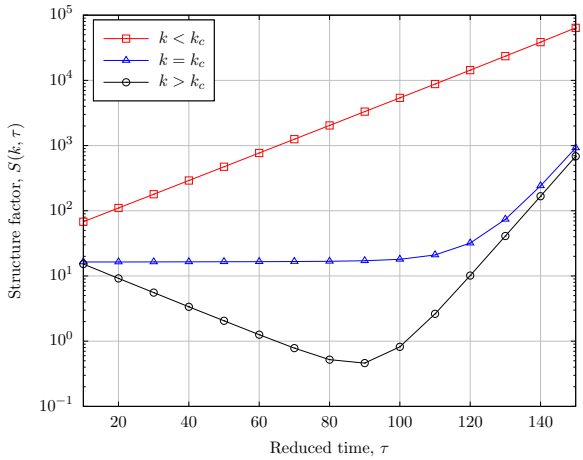

(a) $S(k,\tau)$ at fixed k values

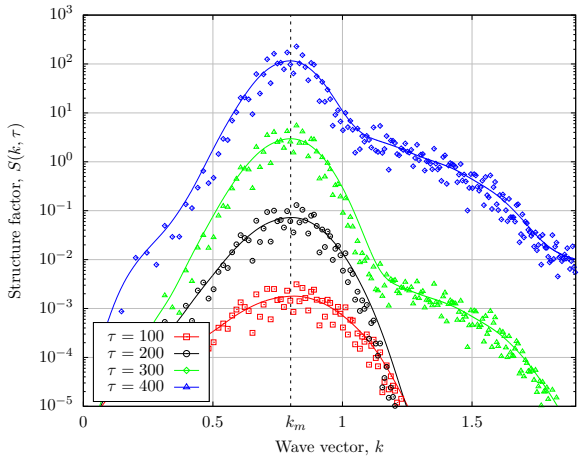

(b) $S(k,\tau)$ at fixed τ values

Figure 2.7: Time evolution of the $S(k,\tau)$ structure factor, and demonstration how k_c cutoff wave vector and k_m maximum wave vector can be determined from it. These simulations were performed with the SKMF model for a phase separating silver-copper alloy. The initial state was a homogenous system having $\bar{c} = 0.3$ average concentration, with additional small initial concentration fluctuations of the amplitude of 0.002.

$$\lambda_c = \sqrt{\frac{8}{2\frac{V_0}{kT} - 6\frac{V_1}{kT}(1-2c) - \frac{1}{c(1-c)}} \frac{\kappa_R}{kT}}\pi. \tag{2.29}$$

Figs. 2.8 (a) and (b) show this function calculated for the regular $V_1 = 0$ and non-regular $V_1 \neq 0$ solution case. It can be clearly seen that the results of these SKMF simulations agree well with the analytical calculation in the regular case, but show a different behavior with respect to the non-regular solution.

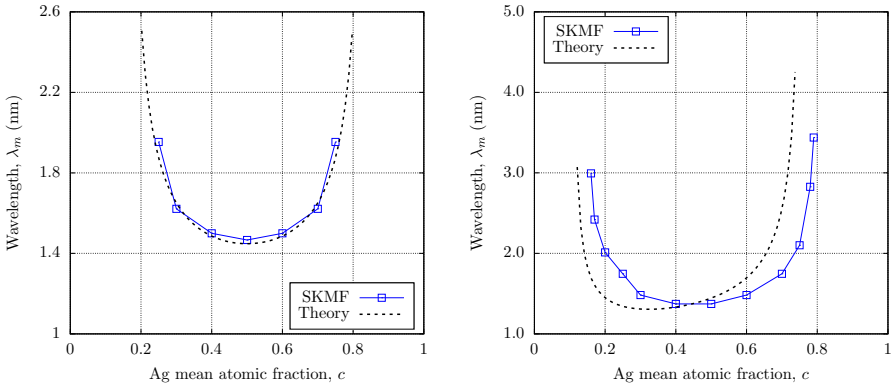

(a) $\lambda_m(c)$ at $V_1 = 0$ (b) $\lambda_m(c)$ at $V_1 \neq 0$

Figure 2.8: The λ_m maximum wavelenths based on analytical and model calculations for phase separation in the Ag-Cu alloy. The initial state of these three dimensional simulations were homogeneous alloys with random initial composition fluctuations of amplitude 0.002. The calculations were started from different inital mean $\bar{c}$ concentration values, at $T = 873$ K temperature, (a) $V_1 = 0$ (regular solution), (b) $V_1 \neq 0$ (non-regular solution). The solid lines being only guides to the eye.

The explanation for this discrepancy can be attributed to the fact that the κ gradient energy coefficient in the SKMF model is composition dependent in the non-regular case. In contrast, in the analytical calculations presented here Eq. (2.29), the free energy function can be composition dependent without having a composition dependent gradient energy coeffi-

cient. Of course, we could substitute a composition dependent gradient energy coefficient into Eq. (2.29), but that would not be justified because the Cahn-Hilliard equation was derived in a way, to contain only the composition independent gradient energy coefficient.

2.4 Conclusions

In this chapter, spinodal decomposition in the binary Ag-Cu alloy was examined, which has a slightly asymmetric miscibility gap and spindodal curve. Since it is a non-regular solid solution, the relationship between the excess free energy function and the composition cannot be represented as a second-order polynomial, but with a composition dependent interaction energy.

It was shown that the interaction energy assumed to be composition-dependent necessarily leads to a composition-dependent κ gradient energy coefficient. It was also shown that by taking the interaction energy $V(c)$ from the free energy function, an equation can be written for the κ-composition function function: $\kappa = -1/12 r_0^2 \partial[(1-2c)V(c)]/\partial c$.

It should be noted, however, that the last sections did not cover all the implications of assuming a composition-dependent gradient energy coefficient, but examined it only up to a linear dependence, which corresponds to a sub-regular solid solution. Nevertheless, significant differences were observed for the system by making this assumption. It was demonstrated that the cutoff wavelength of the spinodal decomposition changes, while the equilibrium interface and the solubility curve remains almost unaffected under the influence of the composition-dependent κ .

It was also discussed, that the analytical expression often used to determine the cutoff wavelength is only true for composition independent κ, because it does not take $\kappa(c)$ into account. We improved the SKMF model to include this behaviour with a $V(c)$ composition dependent interaction energy.

Chapter 3

A multiscale procedure

In this chapter a sequential multiscale (MS) procedure is proposed: the SKMF and PFM methods are used on their own natural length scale (atomistic and mesoscopic respectively) and are connected to each other through the upstream transfer of the relevant physical parameters. [1]

The method first consists of combining the length and time scales of SKMF and PFM. This is followed by an atomic-scale simulation of the initial phase of the decomposition dynamics using the SKMF model. The resulting simulation outputs from the early stage dynamics are the inputs of the PFM simulations for the further stage of the process. Finally, by scaling the MS procedure up, a larger box can be simulated using the particle size distribution (PSD) and density as input for the PFM simulations.

The first step in the multiscale process ensures consistent integration of the two models into the global approach. It also ensures that the spatial and temporal scales of the MS procedure are calculated in real units. This coupling of SKMF and PFM was made by examining the growth of a spherical nucleus. The SKMF atomistic model carries its own length scale

[1] This chapter is based on the article B. Gajdics et al. A multiscale procedure based on the stochastic kinetic mean field and the phase-field models for coarsening. *Journal of Applied Physics*, 126(6):065106, 2019. [31]

in real units through its three-dimensional grid. In contrast, the resolution of the PFM is determined by the spatial correlation length ($\simeq l_0$). This characteristic length scale will therefore be the point of connection between the two methods. Related to the natural length scale of the SKMF model, the two methods simulate the interface profiles of the copper-rich precipitates and the silver-rich matrix. The time scales of SKMF and PFM are then combined by monitoring the time evolution of the precipitate radius in both cases. The estimation of the interatomic diffusion coefficient of the Ag-Cu alloy, calculated in a previous work [10], is also used to express the time scale of the MS procedure in real units.

The second step of the MS procedure is to feed atomic simulations of SKMF into the PFM. In this case, the SKMF and PFM simulations are run on simulation boxes of the same size (168^3 grid points in this chapter) at the time point corresponding to the maximum number of precipitates. This strategy is nevertheless limited by the computational load of SKMF simulations if a large simulation box is taken. To scale up the MS procedure, we then use the PSD and the density of precipitates at the maximum number of particles provided by SKMF as an input to the PFM simulations on a larger simulation box (512^3 in this chapter).

3.1 Choosing the parameters for the MS procedure in case of Ag-Cu

In this chapter, we used a modified version of a original SKMF model that can be applied to asymmetric phase diagrams [17], such as Ag-Cu. To this end, the expression for the jump frequency of $\Gamma_{i,j}^{\mathrm{MF}}$ has been modified, based on (1.61), (1.62) and (1.63). This can be done in the equation 2.10 by replacing the constant parameter V_0 with a composition-dependent parameter $V(c)$, which can be defined as follows:

$$V(c) = V_0 + V_1(2c - 1), \tag{3.1}$$

where the two coefficients $V_0(T)$ and $V_1(T)$ can be extracted, for example, from the Redlich-Kister polynomials used in CALPHAD. This reproduces the experimental solubility limits of the alloy. With this, the excess internal energy:

$$\Delta u_{ex}(c) = c(1 - c)[V_0 + V_1(2c - 1)]. \tag{3.2}$$

Thus, the stationary states of the SKMF model give the same asymmetric solubility limits if:

$$V(c_{ij}) = V + V'(2c_{ij} - 1), \tag{3.3}$$

where $V = V_0/Z$, $V' = V_1/Z$ (V_0 and V_1 are defined in Eq. (2.11) for one atom, while V and V' are calculated for one bond), and:

$$c_{ij} = \frac{1}{2(Z+1)} \left[c_i + \sum_{\substack{l=1,\\ l\in\mathcal{V}(i)}}^{Z} c_l + c_j + \sum_{\substack{l=1,\\ l\in\mathcal{V}(j)}}^{Z} c_l \right], \tag{3.4}$$

this is how the interaction energy $\widehat{E}_{i,j}$ shown in the equation (1.63) turns into:

$$\begin{aligned} \widehat{E}_{i,j} = (M - [V + V'(2c_{ij} - 1)]) \sum_{\substack{l=1,\\ l\in\mathcal{V}(i)}}^{Z} c_l \\ + (M + [V + V'(2c_{ij} - 1)]) \sum_{\substack{l=1,\\ l\in\mathcal{V}(j)}}^{Z} c_l. \end{aligned} \tag{3.5}$$

In this chapter, we used the SKMF model to study the kinetics of the phase separation of the Ag-Cu immiscible alloy on the atomic scale. The

Ag-Cu system has an asymmetric phase diagram [24], and consequently the expression (3.5) can be applied for calculating the interaction energy.

The thermodynamic data are from the CALPHAD database, which is used to fit the solubility limits of the system obvserved by experiments [24]. In addition, Ag and Cu have very similar tracer diffusion coefficients in silver, copper, and in the silver-copper alloy [10,32]. Consequently, the value of the diffusion asymmetry coefficient M is chosen to be 0. In addition, the FCC grid is made up of 168^3 grid points, and periodic boundary conditions were applied. Eq. (1.54) is solved in a reduced form using reduced timestep $\Delta t^* = \Delta t \Gamma_0$, reduced noise amplitude $A_n^* = A_n/\sqrt{\Gamma_0}$, reduced fluxes $J_{i,j}^* = J_{i,j}/\Gamma_0$, furthermore M, V and V' are used in $k_B T$ units. The value of the reduced time step is $\Delta t^* = 0.01$, which determines the reduced time of the SKMF simulations. This is t^*_{SKMF}, which can be calculated as the product of the number of iterations and the time step. Also, when dynamic noise is applied (nucleation and growth), the value of the reduced amplitude is $A_n^* = 0.35$.

3.1.1 Solubility limits of the Ag-Cu system

The solubility limits of the Ag-Cu alloy can be calculated for both the SKMF and PFM models, taking the maximum and minimum values of the bulk concentration. In both cases, the criterion for achieving steady-state concentration in the precipitation and matrix was the stationarity of the numerical solubility limits. To meet this criterion, approximately 30,000 iterations were required for the SKMF model and 5,000 for the PFM model. The results of SKMF and PFM are summarized in the Figure 2.3, with blue squares and red circles (full marks). In contrast, the experimental binodal curve of [24] (solid line) can be seen.

The solid Ag-Cu within the temperature range of ($T < 1050$ K) for both models shows a good agreement with the solubility limits of the phase diagram, based on experimental values. This seems reasonable given the

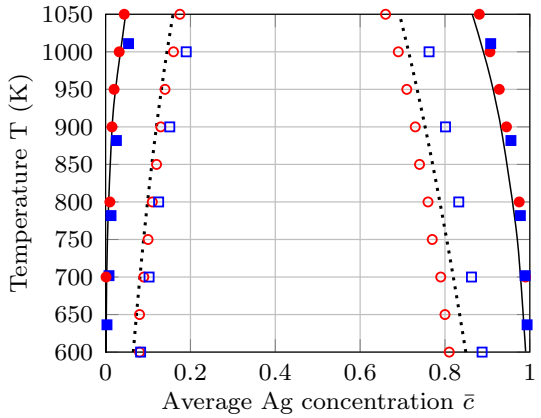

Figure 3.1: Solubility limits (full marks) and spinodal limits (sempty marks) given at different temperatures of the Ag-Cu system, PFM (red circles) and SKMF simulations (blue squares), together with the binodal line provided by the CALPHAD database (black line) and the spinodal line obtained from the Cahn-Hilliard linear theory (black dots).

fact, that the free energy density of the mean-field Bragg-Williams theory, determining the state of equilibrium for the PFM, and the corresponding equilibrium in the SKMF model were parametrized by taking data from the CALPHAD database. he asymmetric nature of the phase diagrams derives from here.

The spinodal curves were also computed for both SKMF and PFM and simulations were done by taking different initial average compositions in a wide range of temperatures. As the initial condition for the PFM simulations, homogenous binary solutions with a small imposed concentration fluctuations with the amplitude of 0.002, a so called static noise. Similarly, homogenous systems were investigated also with the SKMF model, where for a single site a 10^{-6} initial fluctuation was used and the dynamic noise was tuned to zero in these cases ($A_n = 0$). During the mapping of the concentration-temperature field, only such pairs were considered to be within the spinodal curve, which were allowing phase separation to take

place inside the system. Incidentally, this procedure allowed to circumscribe the nucleation-growth domain of the Ag-Cu system. These simulations resulted in slightly different compositions than the theoretical values of the Cahn-Hilliard linear theory (dotted line) for both PFM and SKMF. At least one of the reasons for this difference in the case of SKMF, namely the composition dependence of the gradient energy coefficient, is described in Chapter 2. In the next sections, computer simulations were done using the average initial composition of $\bar{c} = 0.83$, at $T = 873$ K absolute temperature. With these parameter settings, the investigated systems are outside of the spinodal curve for both SKMF and PFM, which places them inside the nucleation-growth domain.

3.1.2 Space scale

In the SKMF model, the length scale is set by the distance between the grid points. In the Ag-Cu alloy, the lattice parameter of the FCC grid is about $a_0 = 0.38$ nm [21], so $\Delta x = a_0/2 = 0.19$ nm. As a result, the simulation grid (168^3 locations) used in SKMF roughly corresponds to a $(32\text{ nm})^3$ spatial volume. In the phase field model, the length scale is determined by adjusting the correlation length using an atomistic approach, a role filled by the SKMF model here. It is worth noting that in reality, the lattice constant changes during decomposition because it is 0.3597 nm in pure Cu and 0.4079 nm in pure Ag [33]. During the simulations, the misalignment of the grid was neglected and the mechanical stresses were not taken into account. This simplification justifies spherical precipitates in the first approximation, in the Ag-Cu alloy, both in the early phase (coherent precipitates) and in the later phase (semi-coherent precipitates) [10].

To fit the distance scale of the two models, we simulated the growth of a single copper precipitate with the SKMF model at an average composition of $\bar{c} = 0.83$ and a temperature of $T = 873$ K. The equilibrium profile of the resulting Ag/Cu interface in the direction $< 100 >$ is indicated by

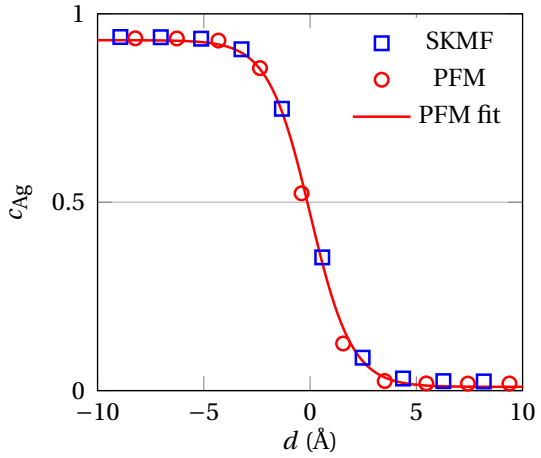

Figure 3.2: Equilibrium profile of Ag/Cu interface for $\bar{c} = 0.83$, at $T = 873$ K. Results by SKMF calculations (blue squares) and by PFM (red circles). Red line shows the fitting of the SKMF results with the typical PFM solution, a tanh function. See details in the text.

blue squares in Figure 3.2. The interface was considered to be in equilibrium when its width and the solubility limits became stationary. At this temperature and composition, the condition was met after roughly 30 000 time steps. A typical hyperbolic tangent function was fitted to the SKMF interface profile that reproduced the PFM composition values well. To be more specific, the interface was fitted by $I(x) = A_0 + A_1 \tanh(x/l_0)$ (correlation factor > 0.999), where the characteristic distance was found to be $l_0 = 0.196$ nm (red line in Figure 3.2). The choice to take $\Delta t^*_{\mathrm{PFM}} = 0.97$ thus provides $\Delta x_{\mathrm{PFM}} = \Delta x_{\mathrm{SKMF}} = 1.90 \times 10^{-10}$ m (see Table 3.1). Though uncommon, this small space step in the PFM is the price to pay if we want to fit the atomic scale composition profile of SKMF with the continuous and differentiable functions solving the phase-field equation (1.15). It is worth mentioning that similar values were used in previous PFM based MS procedures [10, 34]. However, this does not endorse the applicability of PFM on the atomic scale.

SKMF	PFM
$\Delta t = 9.03 \times 10^{-6}$ s	$\Delta t = 6.32 \times 10^{-5}$ s
$\Delta x = 1.90 \times 10^{-10}$ m	$\Delta x = 1.90 \times 10^{-10}$ m

Table 3.1: Smallest discrete units of the space and time scales for SKMF and PFM, at $T = 873$ K.

To verify the transferability of composition profiles from atomistic SKMF to continuous PFM, the SKMF must be run until a state of the appropriate smoothness interface profile is generated, which can be used as a starting point for PFM calculations and the phase field to solve equations numerically. Previous work has shown that continuum equations are also valid on the atomic scale, in cases when the diffusion distance exceeds a few times the distance between the atoms [35, 36]. However, it is important to note that this distance depends significantly on the asymmetry of the diffusion (the dependence of the diffusion coefficient on the composition) [37,38]. In the case of the Ag-Cu alloy examined here, this is actually neglected for the diffusion asymmetry, i.e. the parameter M is considered to be zero in this case. The running times of SKMF calculations were adapted to this condition. This is particularly confirmed by the fact that the concentration profile generated in SKMF simulations is very similar to the hyperbolic tangent profile of PFM, although no Fickian continuous diffusion is assumed in it.

Considering these conditions, a simulation volume of 168^3 was chosen for both the phase field and the SKMF model. The size range thus examined corresponds to approximately $(32\ \text{nm})^3$. The obtained phase field concentration profile is shown in the Figure 3.2 marked with red circles.

From the value l_0, the gradient energy coefficient κ can be calculated using the formula $\kappa = k_b T l_0^2$. As a result, $\kappa = 4.6 \times 10^{-21}\text{J nm}^2$ or otherwise $\kappa = 2.1\text{eV nm}^{-1}$ at a temperature of $T = 873$ K, where the density is taken as 72.9nm^{-3} for the Ag-Cu alloy. This value is slightly larger than

the $\kappa = 1.5\text{eV nm}^{-1}$ obtained in Monte Carlo / molecular dynamics simulations in the work [10] at $T = 900$ K. Also, the SKMF interface profile is slightly stiffer than the system state projected in the previously mentioned article. Here, moreover, it was found that in the temperature interval between 600 and 1000 K, the gradient energy coefficient is independent of temperature. Therfore, we propose that this constant κ value can be used to back-calculate the l_0 length scale at any temperature in this temperature range.

3.1.3 Time scale

To calculate the real time scale t_0 for the Ag-Cu binary alloy, it is first necessary to determine the atomic mobility $\mathcal{M}$. This can be done based on Martin's model, which is suitable for bulk diffusions in two-component alloys [11]:

$$\mathcal{M} \simeq \frac{\bar{c}(1-\bar{c})}{k_B T}\bar{D}, \tag{3.6}$$

where $\bar{D}$ denotes the chemical interdiffusion coefficient. This is assumed to be independent of the composition of Ag and Cu near the transition between the matrix concentrations. This is also evidenced by the fact that the tracer diffusion coefficient is close to that of Cu, Ag and Ag-Cu. This choice does not contradict the assumption that the diffusion asymmetry parameter in SKMF was chosen to be zero in the equation (1.63). In line with these, the chemical interdiffusion parameter in [10] is as follows: $\bar{D}(T = 873$ K $) = 75.9\text{nm}^2\text{s}^{-1}$. The value of the atomic mobility can then be evaluated at $T = 873$ K temperature. Using the formula (3.6): $\mathcal{M} = 161\text{nm}^2\text{s}^{-1}\text{eV}^{-1}$. Thus, for the PFM, the time scale is $t_0 = l_0^2/(k_b T\mathcal{M}) = 3.16\ 10^{-3}$ s. This t_0 will also give the multiscale procedure's time scale.

In order for the SKMF model to be consistently incorporated into the multiscale method, its time scale must first be linked to the phase field

model. This was done by numerically simulating the growth of a single precipitate for both models, where the temperature was chosen to be $T = 873$ K and $\bar{c} = 0.83$ was the mean concentration of the system. The mid-point of the interface between the matrix and the precipitate was taken to estimate the radius of nucleus. The precipitate's radius at the initial state was approximately 20 atomic distances, i.e. $R(t = 0) = 3.8$ nm. This is much larger than the critical radius required for nucleation. In addition, a concentration of 0.013 was used for both models for the precipitate, which is determined by the lower solubility limit of the alloy. This initial state is indeed the same as the equilibrium shape of the precipitate in study. Thus, in the calculations, the growth is examined by the Fick diffusion approximation, except for the initial steps adjusted to the equilibrium profile, as shown by Fig. 3.2. In the SKMF simulations, the noise amplitude was chosen to be zero, thus facilitating easier comparison with the phase field model.

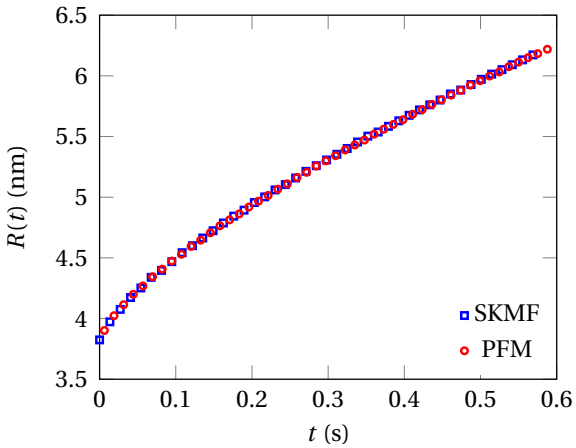

Figure 3.3: The growth of a single precipitate's radius $R(t)$, where $T = 873$ K and $\bar{c} = 0.83$. The result obtained from the SKMF simulation is shows with blue squares and the corresponding PFM result with red circles. Here, SKMF time scale was rescaled by a factor $\tau_0 = 3.50$.

Figure 3.3 shows the results of the SKMF and PFM calculations for the

time evolution of the precipitate radius $R(t)$. The two curves are almost identical except for a multiplication factor of $\tau_0 = 3.50 \pm 0.01$, which shows that the reduced time scale of the two models is proportionally related to each other, so: $t^*_{\mathrm{SKMF}} = \tau_0 t^*_{\mathrm{PFM}}$. Consequently, the time scale of the SKMF model can be converted using the real-time scale of PFM t_0 determined by atomic mobility $\mathcal{M}$. This results in the Figure 3.3. Another possible solution is to estimate the real time scale in the SKMF model itself using the expression of the MF jump frequency $\Gamma^{\mathrm{MF}}_{i,j}$, as in (1.62) and then compare with the time scale of PFM t_0. Here, however, we decided to use the same time scale for both methods, which allows the kinetics of the early and later stages of the system to be compared for SKMF and PFM.

Determining that $\Delta t^*_{\mathrm{SKMF}} = 0.01$ and $\Delta t^*_{\mathrm{PFM}} = 0.02$, the time scales of the two models can be displayed in a common table as shown in 3.1. It should be noted here that the time scale of the PFM model relative to SKMF is about seven times bigger, so: $\Delta t_{\mathrm{PFM}} = 7.00 \times \Delta t_{\mathrm{SKMF}}$. We also performed simulations using dynamic Langevin noise for the SKMF model, in which a similar time scale for a single precipitate growth was obtained. However, due to the stochastic nature of the model, it also allows the appearance of additional nuclei. In this case, therefore, we fitted the time scale of the two models to the temporal evolution of the first precipitate's radius. It should also be noted that the curves in Figure 3.3 conform to the law of the square root of time. This is predicted by Wagner's theory [39] in the case of the growth of a single nucleus, and this supports the assumption that the Fickian approximation of diffusion regime is correct.

3.2 Multi-scale simulation of nucleation and growth in the Ag-Cu system

3.2.1 SKMF simulations

The simulations were performed at 873 K for the SKMF model, where a total of $8.75 \cdot 10^6$ simulation steps were required to examine the copper-rich clusters in the silver matrix. As shown in Figure 3.1, the average composition in the initial state $\bar{c} = 0.83$ is outside the spinodal region but within the miscibility gap for both methods. In order to be able to cross the nucleation barrier, we decided to use dynamic noise. However, it is important to note that the time required for nucleation strongly depends on the chemical driving force on the one hand and on the amplitude of the noise on the other hand. This driving force is significantly weaker for systems where $(\bar{c}, T)$ is closer to the spinodal curve. Also, higher A_n dynamic noise typically results in more viable copper precipitates, however, the statistics will be worse, while higher $\bar{c}$ will lead to longer nucleation time. Figure 3.4(a) shows the formation of the first small precipitates smaller than 1 nm.

The formation of additional nuclei is then observed, and a rapid increase in the average radius occurs $\tilde{R}$ (Fig. 3.5(b)) until the maximum number of copper-rich particles is reached (Fig. 3.5(a)). This time step ($t = 0.16$ s) served as the initial configuration for the phase field simulations. Then we can see a decrease in the number of precipitates and an increase in the radius $\tilde{R}$, which is the result of the coarsening process.

No viable nuclei were observed in the initial stage of nucleation. Figure 3.4(a) shows the early stage of the nucleation process (0.05 s). Thereafter, during a rapid growth phase, the system quickly reaches the state corresponding to the maximum number of precipitates (~ 0.16 s). In this case, the average size of the precipitates is about 1.5 nm. The much slower coarsening process is the next stage where the average radius of nuclei starts to increase (Figure 3.4(b)). Separation can be well characterized by calculating

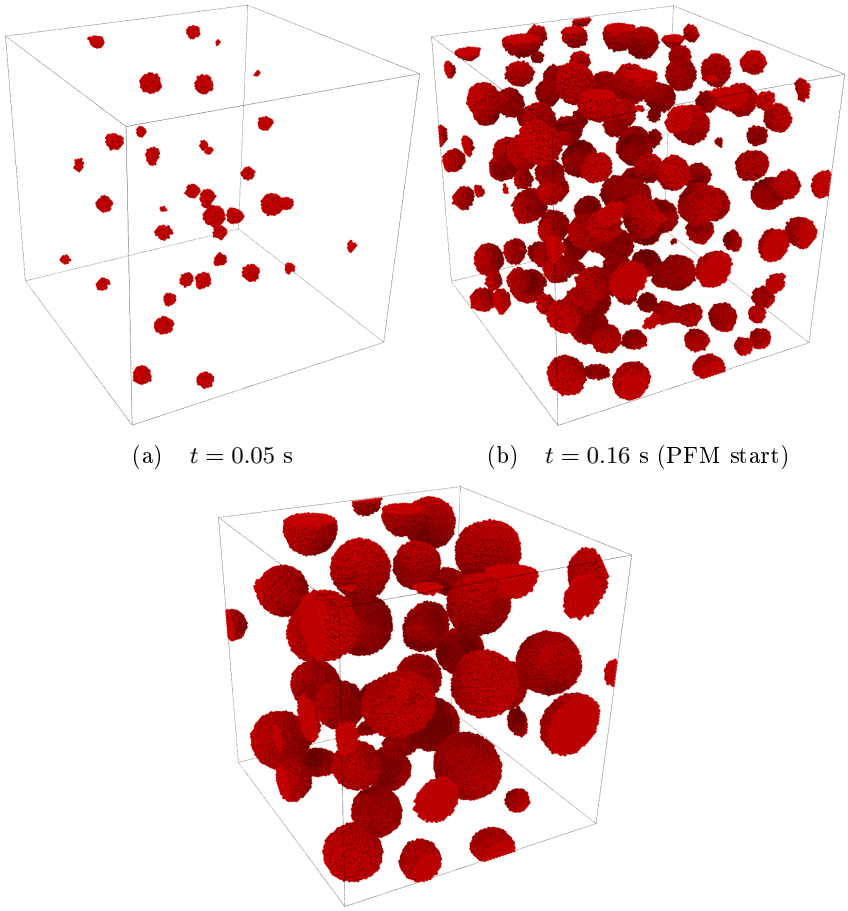

(a) $t = 0.05$ s (b) $t = 0.16$ s (PFM start)

(c) $t = 7.90$ s

Figure 3.4: Resulting microstructures of SKMF simulations. The dynamic noise amplitude A_n^* was 0.35 and $T = 873$ K, $\bar{c} = 0.83$. The corresponding times are a) $t = 0.05$ s, b) $t = 0.16$ s and c) $t = 7.90$ s.

the number of AA, BB, and AB bonds using the atomic finding probabilities in SKMF. If the two neighboring lattice sites are i and j, then $c_i c_j$ gives the number of Ag-Ag, $(1 - c_i)(1 - c_j)$ a Cu-Cu and $c_i(1 - c_j) + (1 - c_i)c_j$ of the Ag-Cu bonds. The formation of the bond between the same sort of atoms (AA and BB) is energetically more favorable, therefore a decrease in

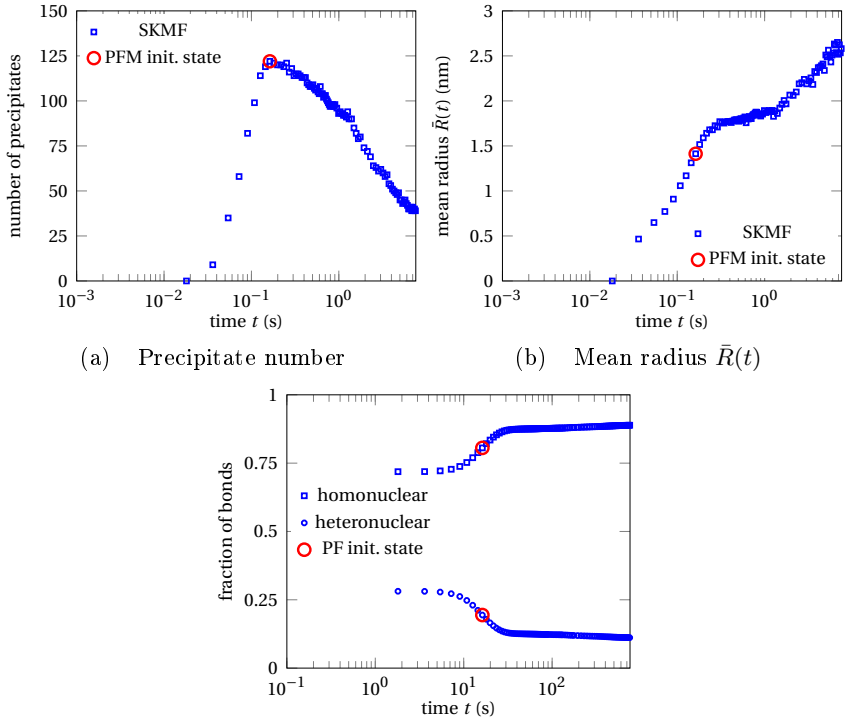

(a) Precipitate number (b) Mean radius $\bar{R}(t)$

(c) Fraction of bonds

Figure 3.5: Results obtained by SKMF simulations (blue squares) for $\bar{c} = 0.83$, at $T = 873$ K temperature and the dynamic noise amplitude was set to $A_n^* = 0.35$: a) total number of nuclei, b) mean radius of the precipitates, c) time evolution of the fraction of homonuclear and heteronuclear bonds in the system. The state, which was chosen as the initial step for PFM simulations is marked with red circles.

the number of unfavorable AB bonds can be observed, as shown in Figure 3.5(c).

3.2.2 PFM simulations

The same temperature and mean composition values were used in the phase field simulations, namely $T = 873$ K and $\bar{c} = 0.83$. The atomic configuration

of the SKMF simulation for the time step $t = 0.16s$ was selected as input for PFM (3.4(b)). Considering that in the SKMF model, the probability of finding atoms varies continuously between lattice sites, during channeling into the PFM model, empty atomic lattice sites were made quasi-continuous by interpolation from adjacent values (Fig. 3.6(a)). It is important to note once again that this connection is based on the method described previously, when the size scales of the two methods were matched by the interface profile of a single-growing precipitate.
It should be noted that in the PFM model, the continuous c coarse grained concentration is discretized on a simple cubic lattice, which is determined at the mesoscopic level. This not only connects the two models by interpolation between the FCC and a simple cubic grid, but also changes the nature of the parameter describing the system. The further study of this question is by no means trivial, but it goes beyond the scope of this work. The maximum number of precipitates is 122 and the corresponding time is $t = 0.16$ s. Figure 3.6 shows how the microstructure of the system changes by PFM simulation. A brief transition state can be observed in the time interval between $t = 0.16$ s and $t \simeq 2$ s . This is followed by the onset of the coarsening regime, where the volume fraction of precipitates is almost constant, while smaller nuclei coalesce or dissolve, and the average radius of larger precipitates increases.

To quantify this observation, we determined the particle size distribution for the system at different time points. This can be seen in Figure 3.7(a). The distribution of the initial state of the PFM simulation can be seen in the insert. One can notice that the distribution begins to flatten over time and shifts in the direction of larger precipitates. The Lifshitz Slyozov Wagner (LSW) theory [40] can be used to describe this behavior, which found that the microstructure of the system is self-similar in the coarsening stage. Therefore, the reduced PSD scaled by the mean radius $\bar{R}$ (red histogram) follows the theoretical distribution of the LSW (black line) in Figure 3.7(b).

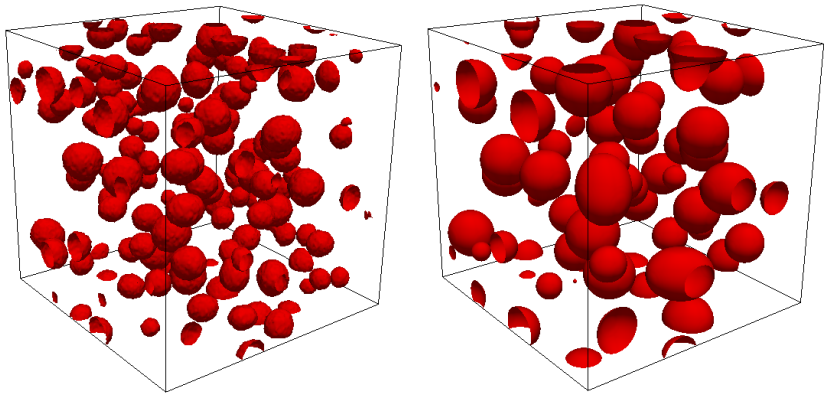

(a) $t = 0.16$ s (PFM start) (b) $t = 2.69$ s

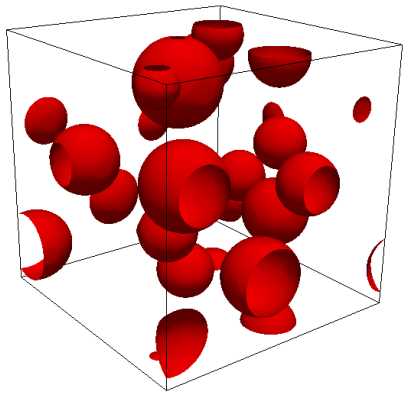

(c) $t = 19.15$ s

Figure 3.6: Results of different stages of the microstructure evolution provided by PFM. The initial composition distribution was taken from SKMF calculations for $\bar{c} = 0.83$, at at $T = 873$ K temperature and $t = 0.16$ s. The system is shown at 3 different time steps of the process: a) $t = 0.16$ s, b) $t = 2.69$ s and c) $t = 19.15$ s.

The change in the number of precipitates and their mean radius over time is plotted in the Figure 3.8. Initially, a rapid decrease in the number of precipitates is observed, while a fast increase is seen in the average radius, which reaches 2.1 nm. This is replaced by a coarsening regime with slower

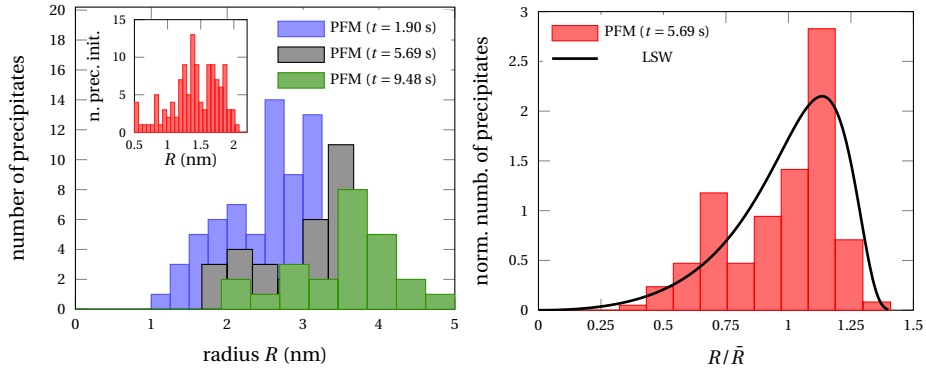

(a) Precipitate size distribution (b) Scaled distribution

Figure 3.7: Distribution of precipitate size provided by PFM computer simulations for $\bar{c} = 0.83$ at $T = 873$ K temperature a) shown at different time steps, where the insert gives the original particle size distribution taken from SKMF simulation, and b) comparison of the theoretical PSD from LSW (black line) and obtained results, scaled by the mean particle radius.

dynamics. Formation of steps can be observed in Figure 3.8(b), which is the result of the coalescence or dissolution of precipitate clusters and in this case the statistics are not suitable. We also compared the results for the time change of the mean radius $\bar{R}$ (red circles) with the law expected from LSW theory $\bar{R}(t) = (\bar{R}_c^3 + Kt)^{1/3}$ (black line). At the beginning of the coarsening phase, $\bar{R}_c = 2.27$ nm is the mean radius, and $K = 2.78\text{nm}^3\text{s}^{-1}$ is the LSW rate constant. In the time range between $t = 1$ s and $t = 10$, the two were fitted (correlation factor > 0.99) and the results provided by PFM are in good agreement with LSW theory.

It should be mentioned, however, that the K rate constant is high here. This is due to the fact that the average composition $\bar{c} = 0.83$ is close to the spinodal curve at $T = 873$ K temperature. It has been shown for systems where the second component is present in large quantities, both by analytical [41–43] and numerical [34, 44, 45] calculations that the rate constant can increase by even an order of magnitude. Furthermore, the

analytical calculations of [42] also projected a broader and more symmetric normalized PSD, than what could be expected from the LSW theory, which is also consistent with the results presented here (see Figure 3.7(b)).

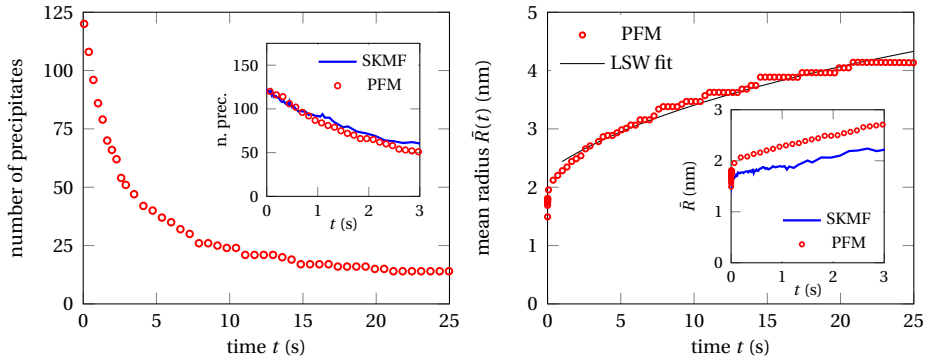

(a) Precipitate number (b) Mean radius $\bar{R}(t)$

Figure 3.8: Results provided by PFM (red circles) simulation: a) change of total number of precipitates and b) mean precipitate radius over time for $\bar{c} = 0.83$, at $T = 873$ K temperature. The black line is the fit based on the LSW theory. The insert contains both PFM (red circles) and SKMF (blue line) results at the early phase of the process.

The confirmation of the MS method's self consistency was done by extending SKMF numerical calculations to the beginning of the early phase coarsening, as it can be seen in Fig. 3.8. Here, one can observe the change in the total amount of nuclei taken as the output of both PFM (red circles) and SKMF (blue line) simulations. In general, the results are matching well at this stage of the process, however the data provided by SKMF shows slightly higher values, than PFM. On the other hand, an approximately constant disparity can be seen on the mean radius measurements. In the case of SKMF, this can be explained by the fact, that a dynamic noise is being present in the course of the computer simulations and thus, even in the coarsening phase of the process, nucleation can still take place. To over bridge this gap and compare the two methods in a more consistent fash-

ion, it would have been necessary to make the comparison between PFM and SKMF in a way that the dynamic noise is being turned off in SKMF after the moment the two simulations were linked to each other ($t = 0.16$ s). This eliminates the further appearance of precipitates, and a thermal equilibrium can be reached inside the silver matrix component. In such a scenario, Ostwald ripending would be the driving process during this stage of the nucleation process. However, the the link created between the two models shows a good agreement and the self consistency of the MS method can be supported.

3.2.3 Upscaling the MS procedure

The next step in the multiscale approach is to feed the particle size distribution (PSD) obtained from SKMF simulations and the precipitate density into the PFM calculations. The downside of the MS method presented so far is the computational cost of SKMF model simulations for large sizes. However, this can be solved by using only the precipitate density and PSD from atomic level simulations and scaling it up for PFM calculations. Thanks to this, we can investigate arbitrarily larger volumes using the PFM. For this purpose, the state obtained at $t = 0.16$ s in case of the SKMF model was taken as the initial configuration, in which 122 precipitates are found in a simulation box of $32\text{nm}^3 = 32768\text{nm}^3$. This, approximately corresponds to a precipitate density of 3.72×10^{-3}. The PFM model calculations were discretized on a 512^3 grid, which is equivalent to a sample volume of 100 $^3\text{nm}^3$. The precipitation density of SKMF at this volume projected 3723 particles for the PFM model, which allowed good statistics. The corresponding Figure 3.9(a) shows the PSD again. 3723 nuclei were generated with a uniform distribution in the volume, and the particle sizes were also chosen randomly, following the PSD of the SKMF model.

For that purpose, the inverse F_R^{-1} of the cumulative distribution function $F_R(r) = \mathbb{P}(R \leq r)$ ($\mathbb{P}$ being the probability) associated to the PSD of SKMF

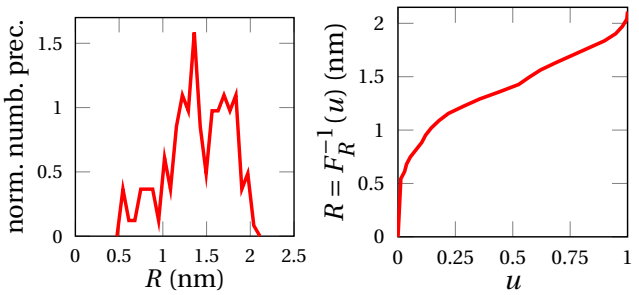

(a) Normalized PSD (b) Inverse partition function

Figure 3.9: a) Initial PSD for PFM upscaled simulations and b) corresponding inverse partition function $F_R^{-1}(u)$ used on a random trial u with uniform law.

was determined (see Fig. 3.9(b)). Then, each particle radius R was drawn as $R = F_R^{-1}(u)$, where u is a random trial of the uniform law between 0 and 1. The evolution of the microstructure simulated by the PFM on a 100^3 nm^3 computation grid is displayed in Fig. 3.10, at times $t = 0.16$ s (PFM initial state), $t = 1.26$ s and $t = 17.7$ s.

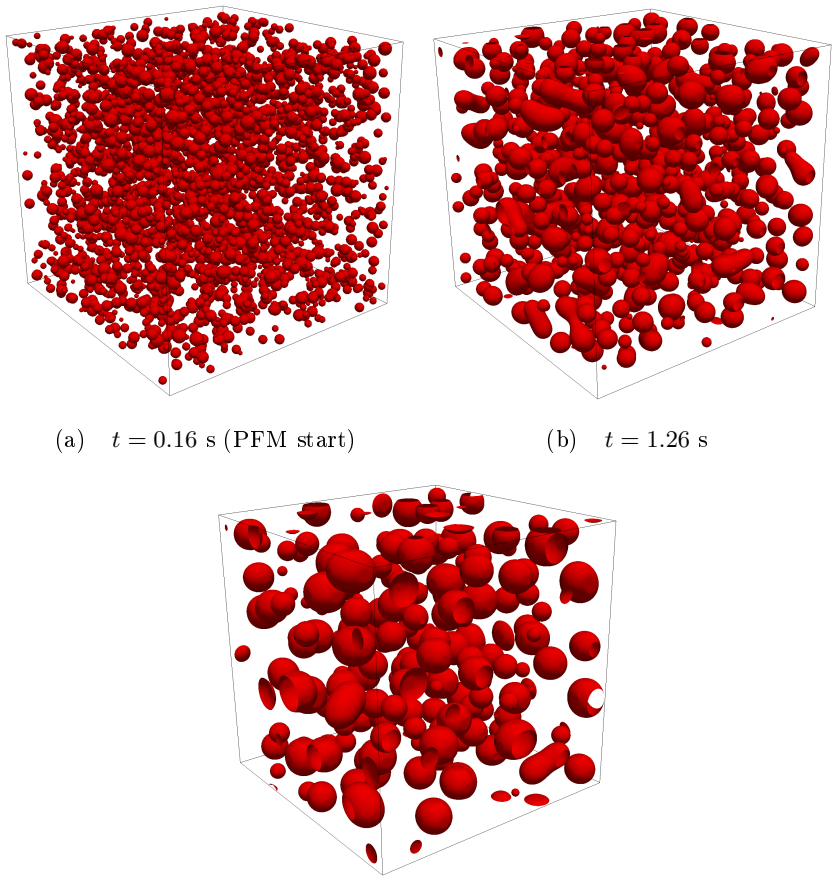

(a) $t = 0.16$ s (PFM start)

(b) $t = 1.26$ s

(c) $t = 17.7$ s

Figure 3.10: Results of PFM simulations calculated using a simulation box consisting of 512^3 grid point. The PSD was taken from SKMF calculations performed on a 168^3 system. $T = 873$ K temperature and $\bar{c} = 0.83$ mean composition was chosen and the corresponding times are a) $t = 0.16$ s, b) $t = 1.26$ s and c) $t = 17.7$ s.

Chapter 4

3DO-SKMF

The following section introduces a computer simulation method that can efficiently study the atomic motion process of three-dimensional objects. This so-called 3D object stochastic kinetic modeling framework (3DO-SKMF) is able to take into account surface segregation as well as the effect of surface curvature (Gibbs-Thomson effect). [1] The created model can simulate objects of any shape in an extremely advantageous and flexible way, as a result of which it can be easily applied to model various nanosystems, such as nanoparticles, nanopillars, nanotubes, nanorods, etc. Similarly to the SKMF model presented in the previous chapters, the stochasticity of the system can be tuned with the help of a noise term. In this chapter, I demonstrate the applicability of the model and I also reproduced experimentally observed results of a phase separating copper - silver nanoparticle using this new framework.

[1] The chapter is based on the following publication: Gajdics et al. An effective method to calculate atomic movements in 3D objects with tuneable stochasticity (3DO-SKMF). *Computer Physics Communications*, 258:107609, 2020. [46]

4.1 New framework

The equations presented in the 1.2.2 section are true only for bulk systems with periodic boundary conditions. However, if we want to examine a sample of any shape, it becomes essential to introduce another approach instead of a periodic boundary condition. This is made possible by creating new equations and making the necessary modifications to the algorithm. In the next section, I present a way of considering surface effects in the new framework.

4.1.1 Equations for 3D objects with free surfaces

A first and simple approach for taking the surface effects into acount for solving our equations can be the so called broken bond model (BBM) [38]. This assumes that a site i, which is located close to the surface, does not have the full set of Z first neighbours, but instead the first coordination shell is being constructed of $Z - B_i$ sites, where B_i denotes the number of broken bonds in the close neighbourhood of site i. Accordingly, Eq. (1.60) interaction energies can be adjusted based on the assumption of the presence of broken bonds:

$$E_s^X = \left[\sum_{l=1}^{Z-B_s} c_l V_{AX} + \sum_{l=1}^{Z-B_s} (1-c_l) V_{BX} \right] . \tag{4.1}$$

The summation runs over the first neighbouring sites, where $Z - B_s$ is the total number of atomic sites in the first coordination shell of site s.

$\Gamma_{i,j}^{\mathrm{MF}}$ exchange rate must be written in a new form, which contains the surface effect:

$$\Gamma_{i,j}^{\mathrm{MF}} = \Gamma_0 \exp\left(\frac{E_{i,j}^S}{\mathrm{k}T} \right) . \tag{4.2}$$

After some algebra, taking into account the BBM [47], one can find that

$E^S_{i,j}$ changes to:

$$E^{S,BBM}_{i,j} = (M-V)\sum_{\substack{l=1,\\ l\in\mathcal{V}(i)}}^{Z-B_i} c_l + (M+V)\sum_{\substack{l=1,\\ l\in\mathcal{V}(j)}}^{Z-B_j} c_l + \tag{4.3}$$
$$+\frac{1}{2}(B_j-B_i)V + \frac{1}{2}(B_j-B_i)M + \left(Z-\frac{B_i+B_j}{2}\right)(V_{AB}+V_{BB}).$$

The $\frac{1}{2}(B_j-B_i)V$ term together with the first two summation terms cause surface segregation due to the chemical interactions between the components. The term $\frac{1}{2}(B_j-B_i)M$ stands for the difference between the surface energies of the system's two components, resulting in surface segregation. Another term was introduced to represent the exchanges rates that are different close to the surface region or in the bulk material and this last piece of the equation does not depend on the composition. In one extreme case, when both B_i and B_j are 0, i.e. the sites do not have any broken first neighbouring bonds, Eq.(4.3) leads to Eq.(1.62) bulk equation. In the plain BBM, the pair interaction energies are creating a bond between the surface segregation and diffusion asymmetry properties of the two components, which reflects in the $M=(V_{AA}-V_{BB})/2$ fourth term of the equation. It must be noted, however, that in real world systems, these are quite often not connected to each other. Such a case is the Ag-Cu binary system, in which the surface segregation is significant [48], but only a slight diffusion asymmetry can be measured [32].

By the introduction of σ^* parameter, which denotes the difference of the specific surface energies between the A and B components, one can avoid to adjust M for the surface segregation:

$$\sigma^* = -\frac{\sigma_A-\sigma_B}{n_0 B_{\text{surf}}}, \tag{4.4}$$

where the surface energies of the A and B components are σ_A and σ_B respectively, n_0 is used to quantify how many atomic sites are located at a

unit surface and B_{surf} show the number of broken bonds for an atom on the material's surface.

Furthermore, in lieu of using the pair interaction energies, in a more phenomenological way, the following equation can be introduced after having understood the role of B_{surf} term in Eq.(4.3):

$$\varepsilon^* = \frac{1}{B_{\mathrm{surf}}} \frac{\ln \Gamma_{\mathrm{surf,surf}}}{\ln \Gamma_{\mathrm{bulk,bulk}}}. \tag{4.5}$$

Here, $\Gamma_{\mathrm{surf,surf}}$ gives us the exchange rate between to surface sites, whereas $\Gamma_{\mathrm{bulk,bulk}}$ is the exchange rate between two neighbouring sites located in the bulk material. Note, that in the case of $\Gamma_{\mathrm{bulk,bulk}}$, none of the sites have broken bonds in their first neighbouring shells. Fig. 4.1 shows the schematic overview of these parameters and demonstrates the relationship between these in a visual manner.

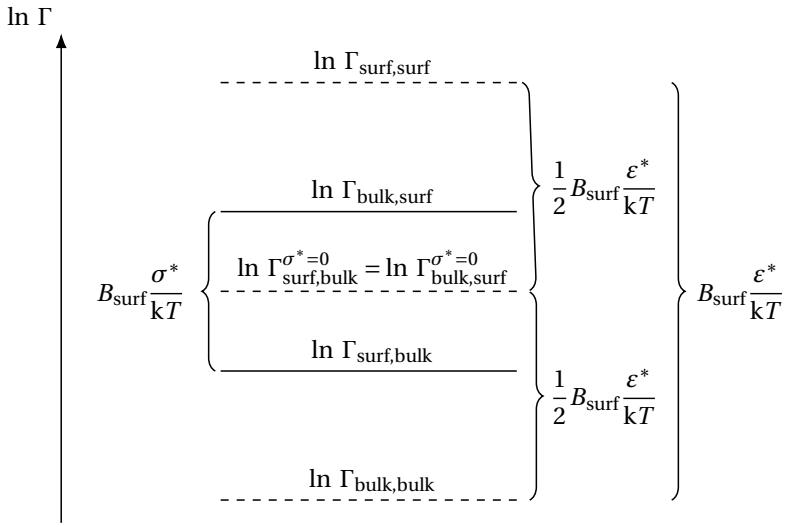

Figure 4.1: Schematic overview of the new key parameters used for 3DO-SKMF calculations and a visual demonstration of the roles of ε^* and σ^*.

Therefore, instead of the original broken bond model, which uses $E_{i,j}^{S,BBM}$, a new equation can be constructed based on the aforementioned observations:

$$E_{i,j}^{S} = (M-V)\sum_{\substack{l=1,\\ l\in\mathcal{V}(i)}}^{Z-B_i} c_l + (M+V)\sum_{\substack{l=1,\\ l\in\mathcal{V}(j)}}^{Z-B_j} c_n + \\ + \frac{1}{2}(B_j - B_i)V - \frac{1}{2}(B_j - B_i)\sigma^* + \left(Z - \frac{B_i + B_j}{2}\right)\varepsilon^*, \tag{4.6}$$

where σ^* is the difference of the specific surface energies of A and B materials, while ε^* controls how fast the diffusion is close to the surface compared to the bulk material. Together with Γ_0 the last term could be viewed as a saddle point energy the value of which depends on the number of broken bonds of the sites involved in the exchange.

4.1.2 Simulation method

This section guides thorugh the description of the method's general arrangement and discusses the necessary technical details of the new algorithm. For better understanding, this section is strictly dedicated to the case of a nanoparticle having a spherical geomety. While solving the main equations numerically, a dimensionless form is being used and thus, the the reduced quantities, which are parameters of this method are the reduced time increment $\Delta\tau = \Delta t\Gamma_0$, reduced amplitude of the noise term $\widetilde{A}_n = A_n/\sqrt{\Gamma_0}$, reduced atomic fluxes $\widetilde{J}_{i,j} = J_{i,j}/\Gamma_0$, moreover M, V, σ^* and ε^* are given in $k_B T$ units, for which the $\widetilde{M}$, $\widetilde{V}$, $\widetilde{\sigma}^*$ and $\widetilde{\varepsilon}^*$ notations are used, respectively. The d lattice distance in the (1 0 0) direction was taken as the unit for the geometrical characterization of the sample and accordingly, the dimensionless radius can be calculated as $\widetilde{R} = R/d$. Fig. 4.2 shows a flowchart of the 3DO-SKMF algorithm and visalizes the main steps of the program.

During the first step of the simulations, the program reads the required

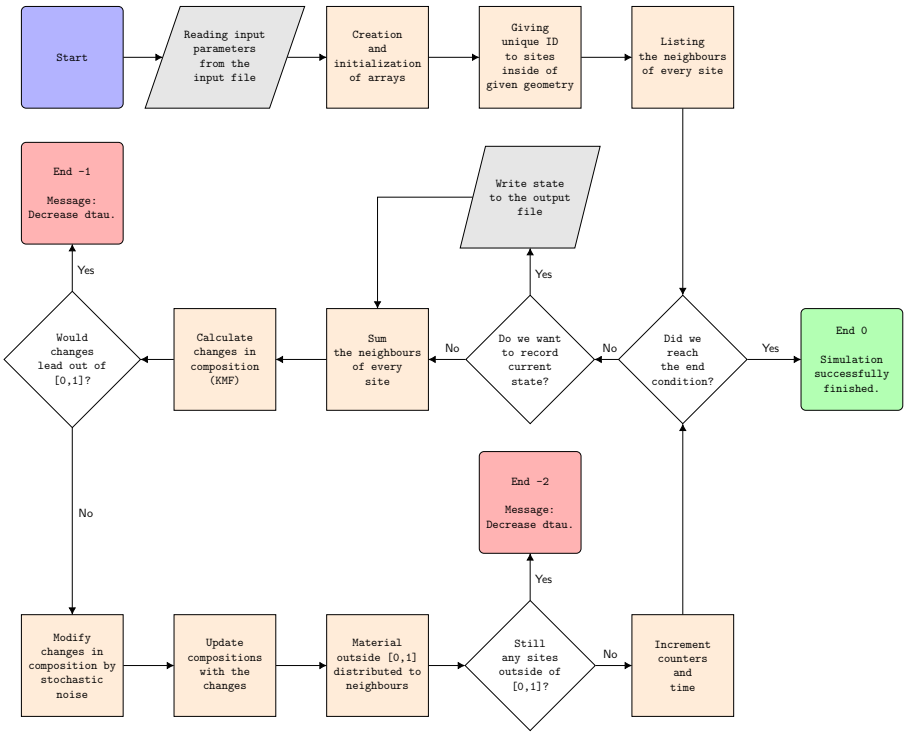

Figure 4.2: Schematic flowchart of the 3DO-SKMF method and overview of the main program steps.

input data form a corresponding file, which contains the system's physical properties, such as $\widetilde{R}$, $\widetilde{M}$, $\widetilde{V}$, $\widetilde{\sigma}^*$, $\widetilde{\varepsilon}^*$ and c_0 initial composition. Additionally, the input file also contains the main parameters of the simulations, $\widetilde{A}_n$, $\Delta\tau$, `Ss` the time delay between records measured in time step units and the `Ns` total number of records required. In Table 4.1 a summary of the necessary input parameters are listed and their corresponding variable names used in the source code.

The next step is to create the arrays needed for the calculations. In the SKMF model presented in the previous chapters, the atomic site with the coordinate `x, y, z` was defined as the element `i, j, k` of the `c` composition

Program variable	**Sign**	**Description**
`M_per_kT`	$\widetilde{M}$	Diffusion asymmetry parameter in kT units
`V_per_kT`	$\widetilde{V}$	Mixing energy parameter in kT units
`An_tilde`	$\widetilde{A}_n$	Noise amplitude in $\sqrt{\Gamma_0}$ units
`dtau`	$\Delta\tau$	Dimensionless timestep in $1/\Gamma_0$ units
`c_start`	c_0	Starting composition
`Eps_per_kT`	$\widetilde{\varepsilon}^*$	Surface diffusion parameter in kT units
`Sig_per_kT`	$\widetilde{\sigma}^*$	Surface segregation parameter in kT units
`r`	$\widetilde{r}$	Inner radius in d units
`R`	$\widetilde{R}$	Outer radius in d units
`L`	$\widetilde{L}$	Length of nanowire or -tube in d units. Value must be even. If set to 0, then the system is spherical.
`Ss`		Frequency of saving data in dtau units
`Ns`		Stop if number of saved states reaches this value

Table 4.1: Input parameters of 3DO-SKMF

array, where the coordinates were natural numbers.

In this framework, the total number of atomic sites in the given volume is `N`, where each site receives a unique identifier between `1` and `N`. In contrast to the previous SKMF model, we do not allocate memory to a coordinate where we do not intend to take the concentration into account, i.e., on an empty atomic site. The FCC structure can be created in such a way that the sum of the absolute values of the coordinates for a given site is an even number. To store these coordinates, three additional `x[N], y[N], z[N]` arrays are created. It must be noted, that the distances are normalised by (1 0 0) planar distance d and choosing the coordinate system according to the base vectors of the FCC lattice, the coordinates are still integer numbers. The memory allocation of these arrays are done dynamically in the source code. Note that although the geometry of the sample can be arbitrary, it is defined through conditions or functions in the program. When constructing a nanoparticle, for example, the atomic sites that fall within a certain sphere radius `R` are included in the arrays and this `R` is also given in d units. The given atomic site then receives the next new unique ID, increasing the size of the dynamic arrays by one, and the value of c_0 is assigned to the concentration array at this element, which is an input parameter to the program. The next step is to search for neighbouring sites in the sample. In order to make this search more optimal, we have built up the allocation of unique ID's following a certain logic. Going from the center of the system, we consider the sites that are within the range of $[R_i; R_i + d)$ distance from the center and repeat this in each cycle. This allows each ID to belong to a specific layer and an array is created for this purpose. The value of the `i`-th element of the array `layer_start[R]` gives us the first ID of the first atomic site from which the `i`-th layer starts.

As already mentioned, after the initialization step, neighbouring sites are searched and stored in additional arrays created for this purpose: `numn[i]` and `nn[i][j]`. The values of the first array are the number of the neigh-

bouring sites of the site i, while the second one stores the ID's of the neoghbouring sites of the given site. These first neighbouring pairs can be easily identified for the FCC structure because these j sites are located at a distance of $\sqrt{2}$ from the site i. One could implement a search algorithm based on this idea for storing the matches found. Although this search only runs once at the beginning of the simulation, as these coordinates do not change during the run, for larger samples this is a rather time consuming and not the least an optimal method. For this reason, we created a more optimized search, in which we search for neighbouring site ID's only in the same layer and in the two adjacent layers. This procedure can be found in the published source code. Of course, we only consider ID's that are larger than the current ID when searching, thus avoiding double-checking of pairs. For the FCC grid, the value of Z total coordination number is 12, which specifies the maximum number of first neighbours. For the atomic sites inside the sample, the number of first neighbours is Z, similarly to the bulk material, while this is not the case near the sample's surface. Here, the `numn[i]` array contains a smaller value than Z. The difference between these is denoted by B_i, which is the number of broken bonds for the given site.

After that, it is the turn of the main computational cycle of the simulation in which the calculation of the kinetic processes takes place.

At the beginning of this loop, we record the current state of the system. Output files are then created with the *.xyz* extension according to the specifications of this format, which is readable by the visualisation software OVITO [49]. This file contains the coordinates and their associated concentration values in the appropriate order and are appended to the end of the file in regular intervals. One can adjust the the total number of saves and the recording frequency in the input file.

For each site i we calculate the sum of the composition of the first neighbours, which is necessary to determine the activation energies from (4.6). The dc_i rate of change of the composition c_i are calculated by (1.54)-

(1.56) and (4.2) and stored. Before updating the `c` array, we need to make sure that that dc_i does not take the value of c_i out of the composition range $[0, 1]$. If this happens, the time step $\Delta\tau$ must be reduced in the input file because the KMF cycle is unstable.

Then the dynamic Langevin noise is applied to the system. (1.57) and (1.58), which will affect the previously mentioned determined dc_i values, which are derived from the deterministic calculation. At this point, c array is updated with the dc values affected by the noise. Note that the high amplitude noise and/or extreme system parameters may result in values outside the range $[0, 1]$. To address this problem, the composition redistribution method, in which the excess material is is distributed among the first adjacent sites based on their composition. The details of this method have been discussed in [14]. After the reallocation cycle, the composition array must be checked again. In addition, the time step $d\tau$ must be reduced if values c outside the range $[0, 1]$ remain after the reallocation. The main loop runs until the simulation is terminated or reaches the number of fixed states defined in the input file.

4.2 3DO-SKMF in use

The applicability of the developed technique is demonstrated for some cases: i) a fully miscible binary alloy with surface segregation in spherical nanoparticles and infinite nanotubes, ii) a hemispherical nanoparticle of a phase-separating alloy, e.g. Ag-Cu, iii) an ideal alloy with surface segregation as a hollow nanosphere.

4.2.1 Ideally mixing alloy with surface segregation

The simplest test that can be performed is a spherical nanoparticle with $\tilde{V} = 0$ and $\tilde{M} = 0$, which is an ideal solid solution, without diffusion asymmetry, but by changing the value of σ^*, responsible for the separation

of atoms A or B, on the surface, one can introduce surface segregation.

It can be seen that in this case the chemical segregation does not occur, but the surface segregation effect occurs due to the missing bonds. Simulations were performed in both cases with sites with initial composition $c_0 = 0.5$. As shown in Figure 4.3, a core-shell structure was formed, where the red and blue colors represent the A-rich and B-rich sites, respectively. By changing the sign of $\widetilde{\sigma}^*$ from positive to negative, the the segregating species can be changed.

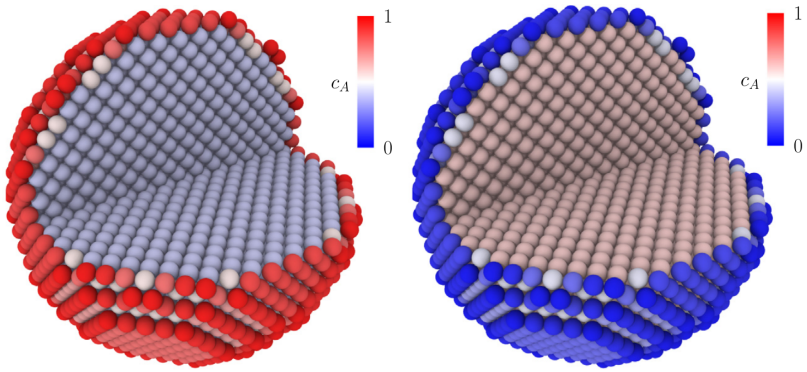

(a) $\widetilde{\sigma}^* = -0.5$ (b) $\widetilde{\sigma}^* = +0.5$

Figure 4.3: Segregation of A and B on the surface of a nanosphere (one quarter removed for visualization) ($\widetilde{R} = 15, c_0 = 0.5, \widetilde{A}_n = 0, \widetilde{V} = 0.0, \widetilde{M} = 0.0$)

Nanowire and nanotube structures can also be simulated using this method. Figure 4.4 shows the results obtained with the formation of a core-shell geometry in an infinite hollow nanotube, where a longitudinally periodic boundary condition was applied but surface segregation was allowed. on the free surfaces (both inner and outer).

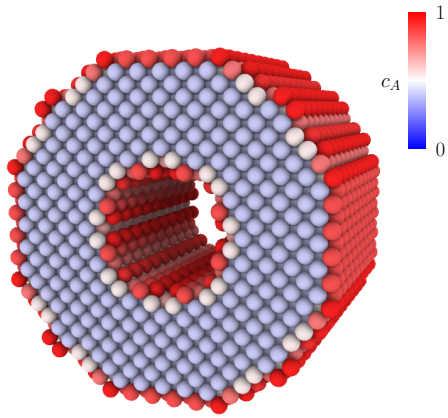

Figure 4.4: Core-shell structure formation in an infinite nanotube ($\widetilde{R} = 10, \widetilde{r} = 4, c_0 = 0.5, \widetilde{A}_n = 0.0, \widetilde{V} = 0.0, \widetilde{M} = 0.0, \widetilde{\sigma}^* = -0.5$)

4.2.2 Phase-separating hemispherical nanoparticle

We investigated spinodal decay in hemispherical nanoparticles and found that formation of a structure similar to the experimentally observed results in Ag-Cu system after codeposition [21]. Figure 4.5(a) shows an Ag-Cu nanoparticle decomposed into Ag- and Cu-rich phases. Figure 4.5(b) is the result of a 3DO-SKMF simulation showing the separation of the A and B phases, (which represent Ag and Cu atoms). The simulation was started from a homogeneous state with the introduction of a small dynamic noise. The resulting composition profiles of the particle cross sections are shown in 4.5(d). As expected, some desegregation is observed near the surfaces due to chemical interaction. Figure 4.5(c) shows that the surface composition values are close to those calculated with the single-layer Fowler-Guggenheim approximation. However, such small changes in composition cannot be detected in microscopic images.

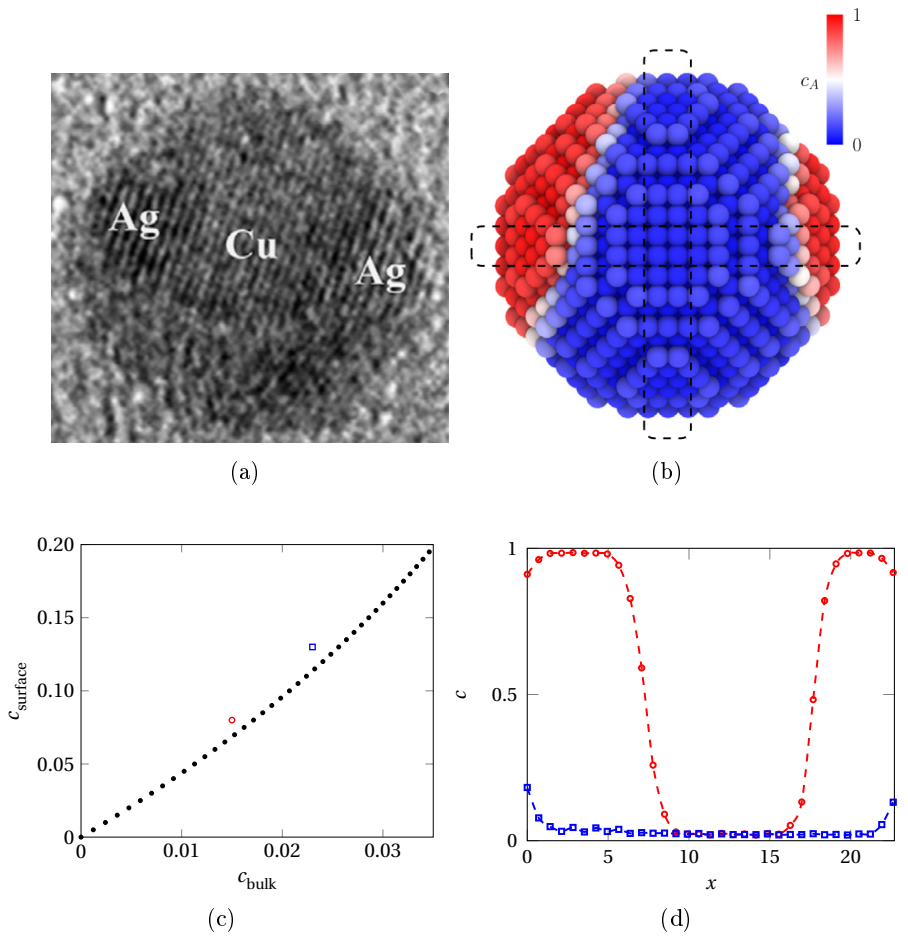

Figure 4.5: Phase separation in a Ag-Cu hemispherical nanoparticle: experimental (a) [21] and the results of simulation (b). The corresponding line concentration profiles are shown in figure (d) ($\widetilde{R} = 12, c_0 = 0.3, \widetilde{A}_n = 0.05, \widetilde{V} = 0.35, \widetilde{M} = 0, \widetilde{\sigma}^* = 0$). In (b), the dashed rectangles represent the areas from which the line profiles were calculated. In (c), we plot the surface compositions as a function of the bulk composition near the sampled surface in two cases. The dashed line shows the prediction using the single-layer Fowler-Guggenheim isotherm

4.2.3 Gibbs-Thomson effect in a hollow nanosphere

The Gibbs-Thomson effect usually refers to the change in chemical potential (or vapour pressure) at a curved surface (interface). As a consequence, the surface composition in a multicomponent system is expected to be different from that of a flat surface in the case of a curved interface – the greater the curvature, the greater the difference. [48] This phenomenological explanation needs to be translated into an atomistic interpretation to understand how this effect can be accounted for in an atomistic model.

In an atomistic picture, in the simplest case, a curved surface differs from a flat surface in the number of broken bonds (BB) – the greater the curvature, the greater the difference. Obviously, the chemical potential on the surface is related to the number of BBs, giving rise to the Gibbs-Thomson effect. As the surface segregation effect is also related to the number and type of BBs, it is expected that the curvature – Gibbs-Thomson effect – also affects the surface segregation, i.e. the equilibrium surface composition is curvature dependent.

Once we understand the atomistic picture of the Gibbs-Thomson effect, we can immediately see that the 3DO-SKMF takes this into account. To test and demonstrate this effect, we performed equilibrium calculations for a hollow nanoparticle (Figure 4.6(a)) and a planar membrane (Figure 4.6(b)) with the same composition far from the surface. As can be seen either in these figures or, even more importantly, in the composition profiles derived from them (Figure 4.6(c)), the surface composition on the two surfaces of the flat sample is not different, whereas the compositions on the outer and inner surfaces of the hollow particle are significantly different. We also note that the surface composition of the membrane is in between the outer and inner surface compositions of the hollow particle, which implies that the concave and convex curvature have opposite effects on the surface composition, as expected from the phenomenological Gibbs-Thomson theory.

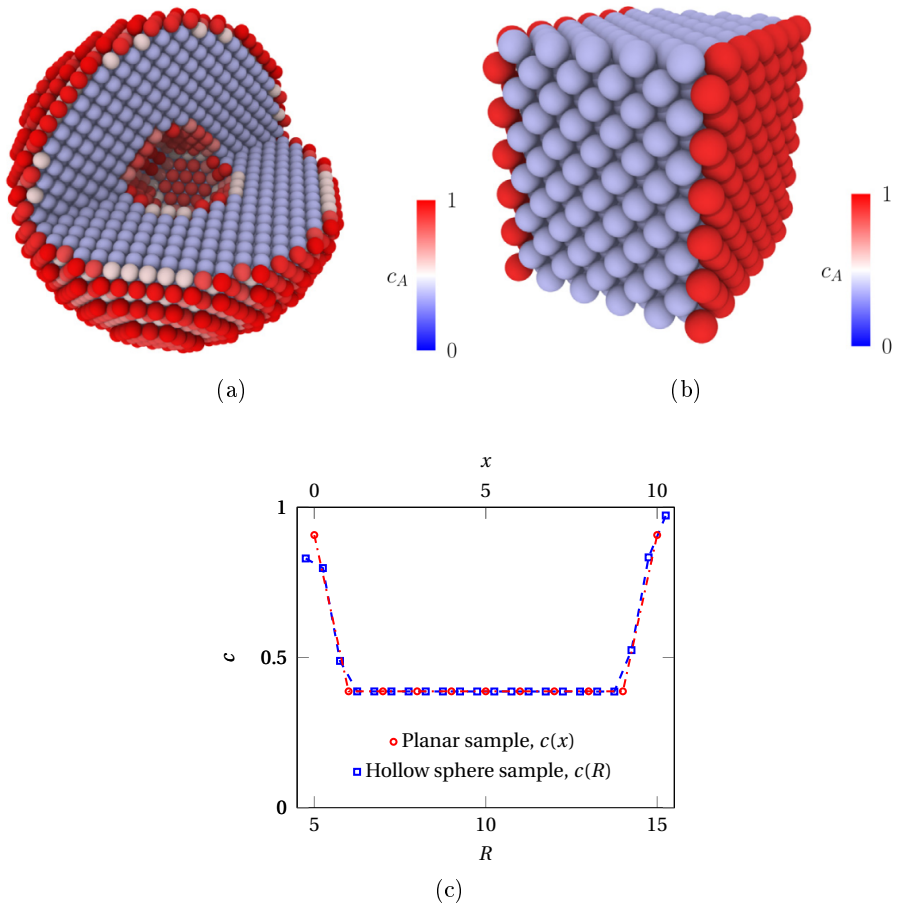

Figure 4.6: Demonstration of the Gibbs-Thomson effect in surface segregation emerging due to the curvature of the surface: (a) hollow nano particle – for better visualisation, a quarter of the particle is removed ($\widetilde{R} = 15.5, \widetilde{r} = 4.5, c_0 = 0.5, \widetilde{A}_n = 0.0, \widetilde{V} = 0.0, \widetilde{M} = 0.0, \widetilde{\sigma}^* = -0.7$), (b) flat membrane ($\widetilde{A}_n = 0.0, \widetilde{V} = 0.0, \widetilde{M} = 0.0, \widetilde{\sigma}^* = -0.7$, starting composition is set to result in the same bulk composition as in subfig. (a)) (c) composition profiles deduced from (a) and (b).

4.3 Conclusion

In this chapter, we have presented an efficient computer simulation method, the so-called 3D Object Stochastic Kinetic Modeling Framework (3DO-SKMF), which is used to calculate the motion of atoms in 3D objects, including surface segregation and the Gibbs-Thomson effect. Thanks to the flexibility and versatility of the model and code, objects of any shape can be easily considered. Accordingly, the model and the computer code can be used in a wide variety of applications: nanoparticles, nanorods, nanotubes, nanocolumns, etc. To increase the versatility of the model, it incorporates stochastic noise in a tunable way. This allows the calculation of processes with activation barriers. To demonstrate the capabilities of 3DO-SKMF, we have presented some examples – flat membrane, nanotube, hollow nanoparticle – and reproduced experimental results showing decomposition in Ag-Cu binary hemispherical nanoparticles.

Conclusion

In my thesis, I presented my contributions in the field of phase separation on the nanoscale by the development of atomistic models and new computer simulation techniques.

1.1. In order to better understand the asymmetric miscibility gap of binary systems, I demonstrated that gradient energy coefficient-composition function $\kappa(c)$ can be calculated from the interaction energy $V(c)$ of a solution. The parameters of the free energy functions were taken from the available literature and examined in connection with the Ag-Cu alloy.

1.2. I illustrated that many calculations and computer simulations usually use composition independent κ and the analytical expression for calculating the cutoff wavelength is valid only for composition independent κ. I improved the SKMF model to consider $\kappa(c)$ via a composition dependent interaction energy $V(c)$.

1.3. Using my program code and based on my computer simulation results, I showed that while the composition dependence of κ does not modify the solubility curve and even the equilibrium interface profile hardly changes, the cutoff wavelength for spinodal decomposition does.

2.1. I made a new quantitative multiscale procedure based on the SKMF and PF models to study the nucleation-growth-coarsening process in alloys. To ensure the consistency of the procedure, I explicitly connected the length

and time scales of the two methods on atomic and mesoscopic levels.

2.2. I performed atomistic simulations on spinodal decomposition and nucleation in Ag-Cu alloy using the improved SKMF model. The program code and the data analysing softwares were developed by me.

2.3. I made a statistical analysis of the nucleation-growth-coarsening process. I compared the results obtained from each models to the Lifshitz-Slyozov-Wagner theory.

3.1. I developed the SKMF model further by introducing new surface parameters additionally to the previous bulk parameters, which takes the whole free surface into account by modifying the activation energy, because the original model was only able to handle samples with periodic boundary conditions.

3.2. I created a new modelling framework based on the SKMF model to calculate atomic movements in 3D objects including surface segregation and Gibbs–Thomson effect. Objects with any kind of shapes (nanoparticles, nanorods, nanotubes, nanopillars, etc.) can easily be considered thanks to the flexibility and versatility of the model and code.

3.3. I compared the simulations of this model with experimental observations of Ag-Cu nanoparticles and I showed that the surface composition values are close to the ones calculated from a single-layer Fowler–Guggenheim approximation. I also demonstrated that this method is able to reproduce the Gibbs-Thomson effect.

Összefoglalás

Disszertációmban bemutattam a nanoskálán végbemenő fázisszeparáció területén végzett munkámat, atomisztikus modellek és új számítógépes szimulációs módszerek fejlesztésének segítségével.

1.1. A kétalkotós rendszerek aszimmetrikus oldékonysági görbéjének jobb megértése érdekében demonstráltam, hogy a gradiens energia együttható-összetétel függvény $\kappa(c)$ kiszámítható az oldat $V(c)$ kölcsöhatási energiájából. A szabadenergia függvényeket az elérhető szakirodalomból vettem és az Ag-Cu ötvözet tekintetében vizsgáltam.

1.2. Megmutattam, hogy számos munka gyakran összetétel-független κ-t használ, és a levágási hullámhossz számítására alkalmazott kifejezés csak összetétel-független κ esetében érvényes. Az SKMF modellt továbbfejlesztettem, hogy $\kappa(c)$-t figyelembe vegye az összetételfüggő $V(c)$ kölcsönhatási energián keresztül.

1.3. A programkódomat használva és a számítógépes szimulációs eredményeim alapján megmutattam, hogy κ összetételfüggése nem módosítja az oldékonysági görbét, és az egyensúlyi interfész profilja is alig változik, míg a spinodális szétesés levágási hullámhossza igen.

2.1. Egy új kvantitatív multiskálás módszert készítettem az SKMF és PF modellek alapján ötvözetek nukleációs-növekedési-durvulási folyamatainak vizsgálatára. Az eljárás konzisztenciájának érdekében összekapcsoltam

a két módszer méret- és időskáláját atomi és mezoszkópikus szinten.

2.2. A továbbfejlesztett SKMF modellt használva atomisztikus szimulációkat végeztem az Ag-Cu ötvözetben végbemenő spinodális bomlással kapcsolatosan. A programkódot és az adatelemző szoftvereket szintén én fejlesztettem.

2.3. Elvégeztem a nukleáció-növekedés-durvulási folyamat statisztikai vizsgálatát. A két modellel kapott eredményeket összehasonlítottam a Lifshitz-Slyozov-Wagner elmélettel.

3.1. Továbbfejlesztettem az SKMF modellt, a korábbi tömbi paraméterekhez új felületi paramétereket vezettem be. Az új modell az aktivációs energia módosítása által figyelembe veszi a teljes szabad felületet. Az eredeti modell csak periodikus határfeltétellel rendelkező mintákat volt képes kezelni.

3.2. Készítettem egy új modellezési keretrendszert az SKMF modell alapján háromdimenziós objektumok atommozgási folyamatainak kiszámítására, beleértve ebbe a felületi szegregációt és a Gibbs-Thomson jelenséget. Mindenféle alakú objektumok (nanorészecskék, nanorudaok, nanocsövek, nanoszálak, stb.) könnyen figyelembe vehetőek a modell és programkód rugalmasságának és sokszínűségének köszönhetően.

3.3. Összehasonlítottam ennek a modellnek a szimulációit Ag-Cu nanorészecskék kísérleti megfigyelésével és megmutattam, hogy a felületi összetételek értékei közel vannak az egyrétegű Fowler–Guggenheim modell becsléséhez. Szintén demonstráltam, hogy ez a módszer alkalmas a Gibbs-Thomson jelenség reprodukálására.

Bibliography

[1] J. W. Cahn, J. E. Hilliard, Free Energy of a Nonuniform System. I. Interfacial Free Energy, The Journal of Chemical Physics 28 (2) (1958) 258.

[2] O. Redlich, A. Kister, Algebraic representation of thermodynamic properties and the classification of solutions, Ind. Eng. Chem. (1948) 345.

[3] Z.-K. Liu, J. Ågren, M. Suehiro, Thermodynamics of interfacial segregation in solute drag, Mater. Sci. Eng. A 247 (1998) 222—228.

[4] E. A. Lass, W. C. Johnson, G. J. Shiflet, Correlation between CALPHAD data and the Cahn–Hilliard gradient energy coefficient κ and exploration into its composition dependence, Computer Coupling of Phase Diagrams and Thermochemistry 30 (2006) 42–52.

[5] T. Barkar, L. Höglund, J. Odqvist, J. Ågren, Effect of concentration dependent gradient energy coefficient on spinodal decomposition in the Fe-Cr system, Computational Materials Science 143 (2018) 446–453.

[6] G. Zhang, T. Yang, S. Yang, Y. Wang, Morphological-evolution pathway during phase separation in polymer solutions with highly asymmetrical miscibility gap, Phys. Rev. E 96 (2017) 032501.

[7] N. Ma, S. Dregia, Y. Wang, Solute segregation transition and drag force on grain boundaries, Acta Materialia 51 (13) (2003) 3687 – 3700.

[8] J. W. Cahn, On Spinodal Decomposition, Acta Metall. 9 (9) (1961) 795.

[9] V. L. Ginzburg, L. D. Landau, On the theory of superconductivity, Sov. Phys. 20 (1064) (1950).

[10] G. Demange, L. Lunéville, V. Pontikis, D. Simeone, Prediction of irradiation induced microstructures using a multiscale method coupling atomistic and phase field modeling: Application to the AgCu model alloy, Journal of Applied Physics 121 (12) (2017) 125108.

[11] G. Martin, Atomic mobility in Cahn's diffusion model, Phys. Rev. B 41 (4) (1990) 2279–2283.

[12] N. Storozhuk, K. Sopiga, A. Gusak, Mean-field and quasi-phase-field models of nucleation and phase competition in reactive diffusion, Philosophical Magazine 93 (16) (2013) 1999–2012.

[13] S. Ouannasser, H. Dreyssé, L. Wille, The tight-binding ising model for surface segregation in binary alloys: formalism and applications, in: A. Borghesi, U. Gösele, J. Vanhellemont, M. Djafari-Rouhani, A. Gué (Eds.), C,H,N and O in Si and Characterization and Simulation of Materials and Processes, European Materials Research Society Symposia Proceedings, Elsevier, Oxford, 1996, pp. 127 – 130.

[14] Z. Erdélyi, M. Pasichnyy, V. Bezpalchuk, J. J. Tomán, B. Gajdics, A. M. Gusak, Stochastic kinetic mean field model, Computer Physics Communications 204 (2016) 31 – 37.

[15] http://skmf.eu (2016).

[16] M. Stan, Discovery and design of nuclear fuels, Materials Today 12 (11) (2009) 20 – 28. doi:https://doi.org/10.1016/S1369-7021(09)70295-0.
URL http://www.sciencedirect.com/science/article/pii/S1369702109702950

[17] B. Gajdics, J. J. Tomán, Z. Erdélyi, Composition dependent gradient energy coefficient: How the asymmetric miscibility gap affects spinodal decomposition in Ag-Cu?, Calphad 67 (2019) 101665.

[18] V. M. Bezpalchuk, R. Kozubski, A. M. Gusak, Simulation of the tracer diffusion, bulk ordering, and surface reordering in fcc structures by kinetic mean-field method, Uspekhi Fiziki Metallov-Progress in Physics of Metals 18 (3) (2017) 205–233.

[19] L. Rout, A. Kumar, R. S. Dhaka, P. Dash, Bimetallic Ag–Cu alloy nanoparticles as a highly active catalyst for the enamination of 1,3-dicarbonyl compounds, RSC Adv. 6 (2016) 49923–49940.

[20] S. Li, T. Wei, M. Tang, F. Chai, F. Qu, C. Wang, Facile synthesis of bimetallic Ag-Cu nanoparticles for colorimetric detection of mercury ion and catalysis, Sensors and Actuators B: Chemical 255 (2018) 1471 – 1481.

[21] G. Radnóczi, E. Bokányi, Z. Erdélyi, F. Misják, Size dependent spinodal decomposition in Cu-Ag nanoparticles, Acta Materialia 123 (2017) 82–89.

[22] D. Bridges, C. Ma, Z. Palmer, S. Wang, Z. Feng, A. Hu, Laser brazing of inconel® 718 using Ag and Cu-Ag nanopastes as brazing materials, Journal of Materials Processing Technology 249 (2017) 313 – 324.

[23] J. L. Murray, Calculations of stable and metastable equilibrium diagrams of the Ag-Cu and Cd-Zn systems, Metallurgical Transactions A 15 (2) (1984) 261–268.

[24] P. R. Subramanian, J. H. Perepezko, The Ag-Cu (silver-copper) system, J. Phase Equ. 14 (1) (1993) 62–75.

[25] N. Saunders, A. Miodownik, CALPHAD: Calculation of Phase Diagrams - A Comprehensive Guide, Vol. 1, Pergamon, 1998.

[26] P. Turchi, Ab initio and CALPHAD thermodynamics of materials, LLNL (2004).

[27] A. van de Walle, R. Sun, Q.-J. Hong, S. Kadkhodaei, Software tools for high-throughput CALPHAD from first-principles data, Calphad 58 (2017) 70 – 81.

[28] R. Arroyave, Commentary: Recent advances in ab initio thermodynamics of materials, JOM 65 (11) (2013) 1499–1500.

[29] N. Lecoq, H. Zapolsky, P. Galenko, Evolution of the structure factor in a hyperbolic model of spinodal decomposition, Eur. Phys. J. Spec. Top. 177 (2009) 165.

[30] J. W. Cahn, Free Energy of a Nonuniform System. II. Thermodynamic Basis, The Journal of Chemical Physics 30 (5) (1959) 1121.

[31] B. Gajdics, J. J. Tomán, H. Zapolsky, Z. Erdélyi, G. Demange, A multiscale procedure based on the stochastic kinetic mean field and the phase-field models for coarsening, Journal of Applied Physics 126 (6) (2019) 065106.

[32] D. B. Butrymowicz, J. R. Manning, M. E. Read, Diffusion in copper and copper alloys, Part II. copper-silver and copper-gold systems, Journal of Physical and Chemical Reference Data 3 (2) (1974) 527–602.

[33] W. P. Davey, Precision measurements of the lattice constants of twelve common metals, Phys. Rev. 25 (1925) 753–761.

[34] D. Molnar, R. Mukherjee, A. Choudhury, A. Mora, P. Binkele, M. Selzer, B. Nestler, S. Schmauder, Multiscale simulations on the coarsening of Cu-rich precipitates in α-Fe using kinetic monte carlo, molecular dynamics and phase-field simulations, Acta Materialia 60 (20) (2012) 6961–6971.

[35] R. Ghez, Diffusion Phenomena: Cases and Studies, Springer US, 2010.

[36] Y. Adda, J. Philibert, V. Pontikis, Validity of the diffusion equation at the atomic scale investigated via numerical simulations, Phys. Rev. B 85 (2012) 144121.

[37] Z. Erdélyi, D. L. Beke, P. Nemes, G. A. Langer, On the range of validity of the continuum approach for nonlinear diffusional mixing of multilayers, Philosophical Magazine A 79 (8) (1999) 1757–1768.

[38] Z. Erdélyi, D. L. Beke, Importance of proper choice of transition rates in kinetic simulations of dynamic processes, Phys. Rev. B 70 (2004) 245428.

[39] C. Wagner, Theory of precipitate change by redissolution, Z. Elektrochem 65 (1961) 581–591.

[40] I. M. Lifshitz, The kinetics of precipitation from supersaturated solid solutions, J. Phys. Chem. Solids 19 (1-2) (1961) 35–50.

[41] A. Ardell, The effect of volume fraction on particle coarsening: theoretical considerations, Acta metallurgica 20 (1) (1972) 61–71.

[42] A. Baldan, Review progress in ostwald ripening theories and their applications to nickel-base superalloys Part I: Ostwald ripening theories, Journal of materials science 37 (11) (2002) 2171–2202.

[43] P. Streitenberger, Analytical description of phase coarsening at high volume fractions, Acta Materialia 61 (13) (2013) 5026–5035.

[44] V. Vaithyanathan, L. Chen, Coarsening of ordered intermetallic precipitates with coherency stress, Acta Materialia 50 (16) (2002) 4061–4073.

[45] T. Wang, G. Sheng, Z.-K. Liu, L.-Q. Chen, Coarsening kinetics of γ precipitates in the Ni–Al–Mo system, Acta Materialia 56 (19) (2008) 5544–5551.

[46] B. Gajdics, J. J. Tomán, Z. Erdélyi, An effective method to calculate atomic movements in 3D objects with tuneable stochasticity (3DOSKMF), Computer Physics Communications 258 (2020) 107609.

[47] C. Cserháti, H. Bakker, D. Beke, Kinetics of surface segregation in alloys, Surface Science 290 (3) (1993) 345 – 361.

[48] J. R. Chelikowsky, Predictions for surface segregation in intermetallic alloys, Surface Science 139 (2) (1984) L197 – L203.

[49] A. Stukowski, Visualization and analysis of atomistic simulation data with OVITO–the open visualization tool, Modelling and Simulation in Materials Science and Engineering 18 (1) (2009) 015012.